Experimental and theoretical investigations on GaN nanowall network

A thesis submitted in partial fulfilment for the degree of

Master of Science

as a part of the

Integrated Ph. D. Programme

(Materials Science)

by

Darshana Joshi

Chemistry and Physics of Materials Unit

Jawaharlal Nehru Centre for Advanced Scientific Research

(A Deemed University)

Bangalore, India

March 2012

Dedicated to

My Parents

DECLARATION

I hereby declare that the matter embodied in this thesis entitled **"Experimental and theoretical investigations on GaN nanowall network"** is the result of investigations carried out by me under the supervision of Prof. S. M. Shivaprasad at the Chemistry and Physics of Materials Unit, Jawaharlal Nehru Centre for Advanced Scientific Research, Bangalore, India and that it has not been submitted elsewhere for the award of any degree or diploma.

Keeping with the general practice in reporting scientific observations, due acknowledgement has been made wherever the work described is based on the findings of other investigators. Any omission that might have occurred due to oversight or error in judgement is regretted.

Date:

Darshana Joshi

CERTIFICATE

I hereby certify that the matter embodied in this thesis entitled **“Experimental and theoretical investigations on GaN nanowall network”** has been carried out by Ms. Darshana Joshi at the Chemistry and Physics of Materials Unit, Jawaharlal Nehru Centre for Advanced Scientific Research, Bangalore, India under my supervision. It has not been submitted elsewhere for the award of any degree or diploma. The contents of this thesis have not been submitted to any other university or institute for the award of any degree or diploma.

Date:

Research Supervisor
Professor S. M. Shivaprasad
CPMU & ICMS,
JNCASR, Bangalore

PREFACE

Research advances in III-nitride semiconductor materials and device have led to an exponential increase in activity directed towards electronic and optoelectronic applications. GaN and related alloys have attracted enormous attention due to their wide bandgap and suitability for high temperature, high power and high frequency electronic applications. They have low dielectric constants with high thermal conductivity pathways, exhibit fairly high bond strengths and very high melting temperatures [1-3].

Though flat 2D – films and GaN nanorods have generated enormous research interest over the years, the observation of a nanowall network that is self-aligned, symmetric and epitaxial attracted our attention. This thesis is an attempt to understand the mechanism of spontaneous formation of the nanowall network of GaN using theoretical simulations, and to characterize various structural, magnetic, electronic and thermal transport properties of this scientifically interesting and technologically important nano-structured array and compare them with those of a commercially available GaN epilayer. Several very novel and interesting properties of these materials are observed. In this thesis only a quantitative attempt in understanding these results, mostly speculative, has been made. The work hopes to generate great interest for further studies in establishing the underlying mechanisms of the nanostructure formation and the curious properties they display.

This thesis is divided into five chapters.

Chapter 1:

This chapter gives a detailed account of group III – nitride family, with special focus on Gallium Nitride (GaN) in terms of its fundamental properties and promising applications. Literature background that highlights the challenges in GaN research, limitation to their applications and how these challenges can be addressed in the various nanostructures is discussed. This chapter concludes by presenting the scope and organization of the thesis.

Chapter 2:

This chapter gives the technical details and working principles of various experimental techniques used for growth and characterization of GaN nanowall network in the present work.

Chapter 3:

This chapter presents a detailed analysis of the various properties of nano-wall network compared with a 2-D flat TDI, MOVPE grown 2μm thick GaN epilayer. Results from various characterizations of morphology, crystal structure, electronic, electrical, magnetic and thermal transport properties using XRD, FESEM, PL, AFM, MFM, SQUID, Hall and I-V measurements etc. are presented.

Chapter 4:

In this chapter details of various theoretical methods employed to study the GaN/Al_2O_3 interface, the results of simulations done and the future direction of the theoretical work are presented.

Chapter 5:

This chapter concludes this thesis by giving a summary of results thus obtained and presents an outlook for the further development of GaN based technology by utilizing this GaN nanowall network.

Contents

Chapter 1 3

Introduction 3

1.1 Group III-nitrides 3

1.2 Crystal structure 4

1.3 Substrates and lattice mismatch 5

Fig 1.2: Possible epitaxial relation between III-N and sapphire 7

1.4 GaN: Band gap engineering 7

1.5 Limitations and new approaches 9

1.8 Scope of this thesis 10

Chapter 2 15

Experimental methods 15

2.1 Growth technique: Molecular Beam Epitaxy 15

2.2 Characterization tools 17

2.2.1 Scanning electron microscope (SEM) 18

2.2.2 Energy-dispersive X-ray spectroscopy (EDX), Elemental mapping 19

2.2.3 Atomic Force Microscopy 20

2.2.4 Magnetic Force Microscopy (MFM) 21

2.2.5 Photoluminescence (PL) and Cathodoluminescence (CL) 22

2.2.6 Van der Pauw method - Hall and I-V characteristics 24

2.2.7 Powder X-ray Diffraction 25

2.2.8 X-ray Photoelectron Spectroscopy 27

2.2.9 Magnetic Measurements: SQUID Magnetometer 29

2.2.10 Thermo power measurements 31

Chapter - 3 35

Results and Discussion 35

Properties of the GaN nanowall network 35

3.1 FESEM and EDX (elemental mapping) 37

3.2 XPS measurement 39

3.3 XRD-HRXRD measurements 40

3.4 Characterization of Band Edge emission: CL spectra 44

3.5 Detailed Photoluminescence Analysis 45

3.5.1 Literature background 45

3.5.2 PL for nanowall network 47

3.6 Cathodoluminescence (CL): CL Spectra and CL imaging 50

3.6 .1 Motivation and Literature background ... 50
3.6 .2 CL mapping for nanowall network ... 51
3.7 Hall and I-V measurements ... 54
3.8 Magnetic Measurements ... 56
3.8 .1 Background ... 56
3.8 .2 Results ... 59
Chapter IV ... 74
Theoretical Studies ... 74
4.1 Density Functional Theory (DFT) ... 74
4.2 SIESTA ... 78
4.3 Results ... 79
4.3.1 Interface Calculations ... 81
4.4. Conclusions ... 86
4.5. Future studies ... 87
Chapter - V ... 90
Conclusions and future directions ... 90
References ... 96

Chapter 1

Introduction

Glory, silicon carbide!
Schottky, switch, and polytype
Cree Research and A-T-T,
F-E-T and S-I-T!

Glory! Gallium nitride.
Nakamura and blue light.
Higher current, higher goal.
Thank you, Yoder, thank you all.

(A poem dedicated to the MRS Panel in the fall of 1998, which summarized SiC and GaN-based research in Japan.)

Chapter 1

Introduction

This chapter gives a detailed account of group III – nitride family, with special focus on Gallium Nitride (GaN) in terms of its fundamental properties and promising applications. Literature background that highlights the challenges in GaN research, limitation to their applications and how these challenges can be addressed in the various nanostructures is discussed. This chapter concludes by presenting the scope and organization of the thesis.

1.1 Group III-nitrides

(Al/Ga/In)-N compounds namely AlN, GaN and InN constitute the group III nitride family. These wide bandgap materials posses several remarkable properties that make them particularly attractive for reliable solid state device applications. They have low dielectric constants with high thermal conductivity pathways, exhibit fairly high bond strengths and very high melting temperatures [1-3]. The large bond strengths could possibly inhibit dislocation motion and improve reliability in comparison to other II-VI and III-V materials [1]. In addition, the group III-nitrides are resistant to chemical etching and hence should allow GaN-based devices to be operated in harsh environments [4, 5]. These properties may lead to devices with superior reliability.

The group III-nitrides are ideal for high-power applications and utilization in caustic environments, because they are chemically inert, are resistant to radiation, have large avalanche breakdown fields, high thermal conductivities, and large high-field electron drift velocities [2, 4, 7-9]. The group III-nitrides and their alloys have been fabricated into various high temperature and high-power microelectronic and optoelectronic devices such as passivation barriers, ohmic contacts in integrated circuits, blue light-emitting diodes, candela-class blue-light emitting diodes, green and yellow light-emitting diodes, UV photodetectors, reflector stacks, high electron mobility transistors, heterostructure field effect transistor, metal semiconductor field-effect transistors, and surface acoustic wave devices. Stimulated emission has been reported from optically pumped GaN and AlGaInN alloy double heterostructure films [2-4].

1.2 Crystal structure

Group III-nitrides are known to exist in two distinct crystalline polymorphs, namely wurtzite (space group C^{4}_{6v}-PC_6mc) and cubic zincblende (space group T^{2}_{d}-F43m) polytypes [9]. For bulk III-Nitrides under ambient conditions, wurtzite is the thermodynamically stable structure, while the cubic zincblende phase is metastable and is observed only for heteroepitaxial layers grown on {011} crystal planes of cubic substrates such as GaAs [13], Si [10], SiC [11] and MgO [12]. In these cases the intrinsic tendency to form the wurtzite structure is overcome by the topological compatibility. A third rock salt form for III-nitrides is also possible only under high pressure.

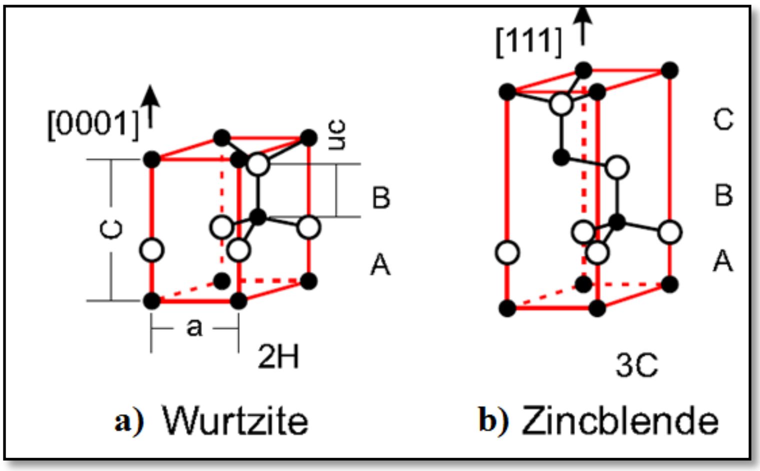

Fig. 1.1 Stick and ball stacking model of crystal with a) with wurtzite structure along the [0001] direction b) Zincblende structure along the [111] direction

Both wurtzite and zincblende structures have tetragonal coordination with each atom bonded to four other atoms of opposite species (Fig.1.1). The nature of the bonding is predominately covalent with some ionic character. Wurtzite structure is a member of the hexagonal close packed system with an ABAB layer structure, and zincblende is cubic close-packed with an ABCABC layer structure. The nearest-neighbour positions are almost identical but the relative positions of the second nearest neighbour differ. The major difference between the two structures is the stacking order of the tetrahedral atomic sheets along the (111) axis. For an ideal wurtzite crystal structure c/a and u parameter values are 1.633 and 0.375 respectively, where u parameter is defined as the anion-cation bond length along c axis. Structure parameters for the group III nitride family are listed in Table 1.1.

Material	Wurtzite (Å)				Zincblende (Å)
	a	c	c/a	u	a
AlN	3.111	4.979	1.601	0.382	4.360
GaN	3.189	5.185	1.627	0.377	4.500
InN	3.538	5.703	1.612	0.380	4.980

Table 1.1: Structure parameters of wurtzite and zincblende structures for group III-nitrides [9, 10, 15-17].

1.3 Substrates and lattice mismatch

The properties of GaN films deposited on foreign substrates depend intricately on the inherent properties of the substrates such as constants of thermal expansion and lattice structure. Process-induced characteristics such as surface preparation and chemical and physical interactions at the surface are also critical. Hence, it is particularly important to employ high quality single crystalline substrates having lattice parameters close to that of group III-nitrides. For this reason, so far, most of the epitaxial growth of nitrides has been performed on sapphire or SiC substrates [19]. In both cases, problems due to the lattice mismatch between the nitride epi-layer and the substrate (16% for sapphire and 3.5 % for SiC) have to be overcome.

Sapphire is one of the most widely used substrate because of its relatively cheap and easy availability, high thermal stability, and feasibility of *in-situ* and *ex-situ* cleaning. Moreover, it is insulating and transparent for most of the bandgaps of nitride alloys; thus it affords certain benefits in optoelectronic devices, for example, for back illumination and in LEDs, for lack of absorption. Sapphire also has similar crystal structure to that of wurtzite group III-nitrides and since it is Al terminated on the surface, it can be easily nitrided to form a thin AlN layer [19].

The lattice mismatch between the substrate and the grown epi-layer is defined as,

$$\frac{a_{III-N} - a_{Sapphire}}{a_{Sapphire}}$$

Where a, is the lattice parameter and subscripts represent the substrate and nitride. There are two possible epitaxial orientations for the group III-nitrides grown on sapphire (0001) surface, which are shown in Fig.1.2. Table 1.2 below shows the lattice mismatch values in the two orientations for different nitrides with sapphire substrate.

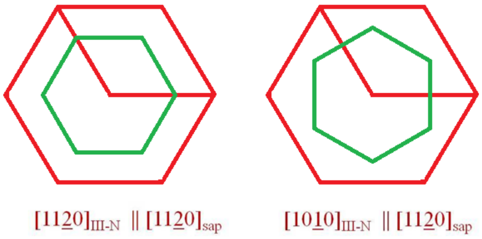
$[11\underline{2}0]_{\text{III-N}} \parallel [11\underline{2}0]_{\text{sap}}$
$[10\underline{1}0]_{\text{III-N}} \parallel [11\underline{2}0]_{\text{sap}}$

Fig 1.2: Possible epitaxial relation between III-N and sapphire.

Material	**Lattice Mismatch**	
	$[11\underline{2}0]_{\text{III-N}} \parallel [11\underline{2}0]_{\text{sap}}$	**$[10\underline{1}0]_{\text{III-N}} \parallel [11\underline{2}0]_{\text{sap}}$**
AlN	-34.6%	+13.3%
GaN	-33.0%	+16.0%
InN	-25.4%	+29.2%

Table 1.2: Lattice mismatch for various members of III-V nitride family for two different epitaxial relations.

1.4 GaN: Band gap engineering

When Johnson et.al first synthesized GaN in 1932, its thermal stability and significant hardness initiated the interest in GaN research. Since then it is the excellent semiconducting features of GaN that have attracted the attention of researchers. Its wide band gap of 3.4 eV [20] allows for numerous applications in optoelectronic and high-frequency devices. For example, GaN makes violet (405 nm) laser diodes possible, without use of nonlinear optical frequency-doubling. Its low sensitivity to ionizing radiation makes it a suitable material for solar cell arrays for satellites. The stability and ease of operation of GaN transistors at high voltages and hotter temperatures as compared to GaAs transistors have opened a wide window of applications in power amplifiers at microwave frequencies [1-3]. GaN can be doped relatively easily as compared to other members of the III-V nitride family to form n-type or p-type films.

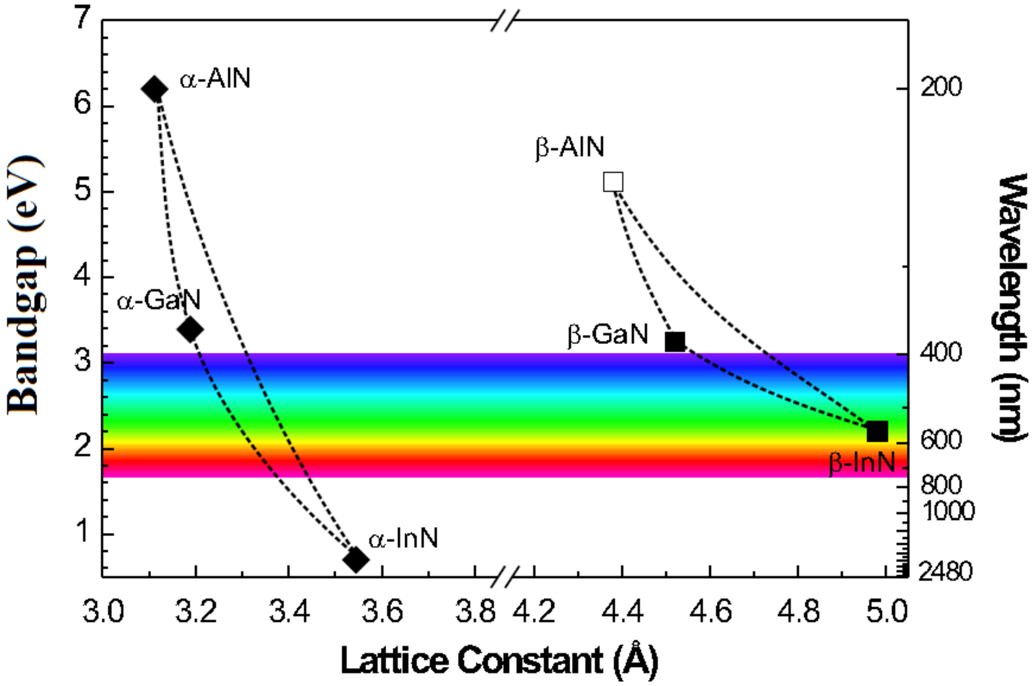

Fig: 1.3 Energy gaps and lattice constants for III-N semiconductors with wurtzite (α-phase) and Zincblende (β-phase) structures.

The wurtzite polytypes of gallium nitride (GaN), aluminium nitride (AlN), and indium nitride (InN) are excellent materials for bandgap engineering, because they form a continuous range of solid solutions and superlattices with direct room-temperature bandgaps ranging from 0.7 eV (InN) [21, 22] to 3.4 eV (GaN) to 6.2 eV (AlN) [21]. Therefore, as illustrated in Fig.1.4, if we alloy GaN with In or Al, depending on the concentration, the full solar spectrum ranging from red, well into the ultraviolet can be spanned. These direct bandgap materials are especially useful as it allows for high quantum efficiency light emitters and full spectrum solar cells to be fabricated in this family of group III-nitrides, by bandgap engineering.

1.5 Limitations and new approaches

Growth of epitaxial device quality group III nitride films with low defect densities and dopant concentrations has been hindered by a lack of suitably lattice matched substrates [19], large n-type background carrier concentrations in the deposited nitride films, and large equilibrium dissociation pressure of N_2 from the nitrides at typical growth temperatures. Regardless of the growth method employed, the major problem in growing group III-nitrides arises from the need to incorporate stoichiometric quantities of nitrogen into the film. Moreover, lack of structural compatibility with the most widely used substrate – sapphire and SiC results in high dislocation density ($\sim 10^{10}/cm^2$), which acts as quenchers for charge carriers and photons. A great deal of effort has been spent in trying to overcome the problems arising from lack of GaN substrates [19]. Some of the best device results have been achieved through the use of buffer layer, epitaxial overlayer growth (ELOG) and lattice matching epitaxy.

So far the focus has been on devices based on epitaxially flat films with low defect densities, which are extremely difficult to form [22-24]. Recent approach has been to form nanostructures of GaN on sapphire that are defect free due to their small sizes and can act as good transporters of electrical and optical carriers [25-27]. Recent developments in the direction to tailor-made nanostructures especially nanorods and nanowalls have shown promising results [28-30]. In this direction, our group has formed a high density ($\sim 10^8/cm^2$) of oriented GaN nanocolums and a hexagonal nanowall network on bare c-plane sapphire by control of growth parameters, without involving lithography, catalysts, buffer layers or nitridation (Fig.1.4) [31,32]. This study performed in nitrogen-rich conditions enables a unique mechanism of strain relaxation, forming a network of nanowalls that promotes supersaturation conditions at open screw dislocations to initiate highly anisotropic one-dimensional (1D) growth. The mechanism suggests that this approach of sheer parametric control can enable tailor-making self-assembled anisotropic materials with desired properties [32]. With narrow growth window for specific morphology fig. 1.5 shows the growth diagram obtained by varying parameters such as temperature, Ga flux and nitrogen pressure.

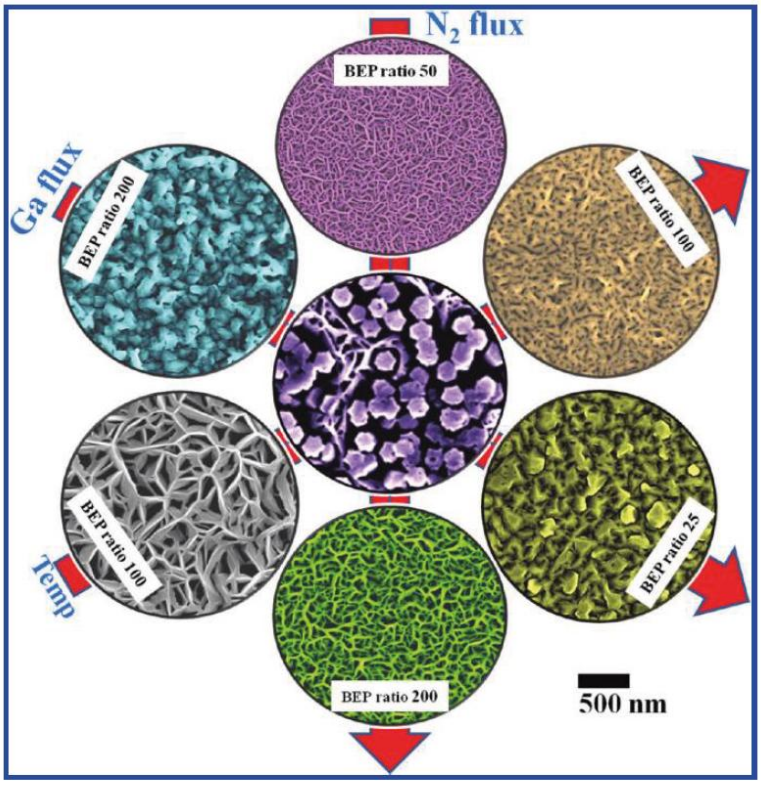

Fig.1.4: Various nanostructures of GaN formed by sheer control of growth parameters (adapted with permission from [*Ref.32*]

1.8 Scope of this thesis

Though flat 2D – films and GaN nanorods have generated enormous research interest, the observation of a nanowall network that is self-aligned, symmetric and epitaxial attracted our attention. This thesis is an attempt to understand the mechanism of spontaneous formation of the nanowall network of GaN using theoretical simulations, and to characterize various structural, magnetic, electronic and thermal transport properties of this scientifically interesting and technologically important nano-structured array and compare them with those of a commercially available GaN epilayer. An attempt to simulate the GaN/Al_2O_3 interface and model the evolution and the super-structure symmetry of interfacial dislocations with film thickness is also made such that these dislocations can be used as nucleation sites for self assembled nanostructure formation. The results show several very novel and interesting properties of these materials. In this thesis only a quantitative attempt in understanding these results, mostly speculative have been made. The work hopes to generate great interest for further studies in establishing the underlying mechanisms of the nanostructure formation and the curious properties they display.

Chapter 2

Experimental methods

Chapter 2

Experimental methods

This chapter gives the technical details and working principles of the various experimental techniques used for growth and characterization of GaN nanowall network for the present work.

2.1 Growth technique: Molecular Beam Epitaxy

Molecular beam epitaxy (MBE) was developed in the early 1970s as a means of growing high-purity epitaxial layers of compound semiconductors. It refers to the well-controlled growth of epitaxial films under ultra high vacuum conditions (~ 10^{-11}torr). The pressure of evaporating species is ~ $10^{-7} – 10^{-9}$torr, so the mean free path of the atoms emitted from the evaporation source, given by the (6/P) relation, is much greater than the size of the chamber. Hence, they travel without being scattered to the substrate where they are rapidly thermalized at the substrate temperature. Fig.3.1 shows a schematic of a typical MBE system. The chamber is cryogenically cooled with liquid nitrogen, which prevents degassing and spurious atoms from bouncing off the chamber walls, therefore acting as a cryopump during growth.

Some of the advantages of MBE over other growth techniques are its clean growth environment, precise control of the beam fluxes and growth condition, easy implementation of *in-situ* characterization instruments, compatibility with other high vacuum, thin-film processing methods (metal evaporation, ion beam milling, ion implantation) etc. An additional advantage of the MBE process is that the clean environment minimizes unintentional doping effects.

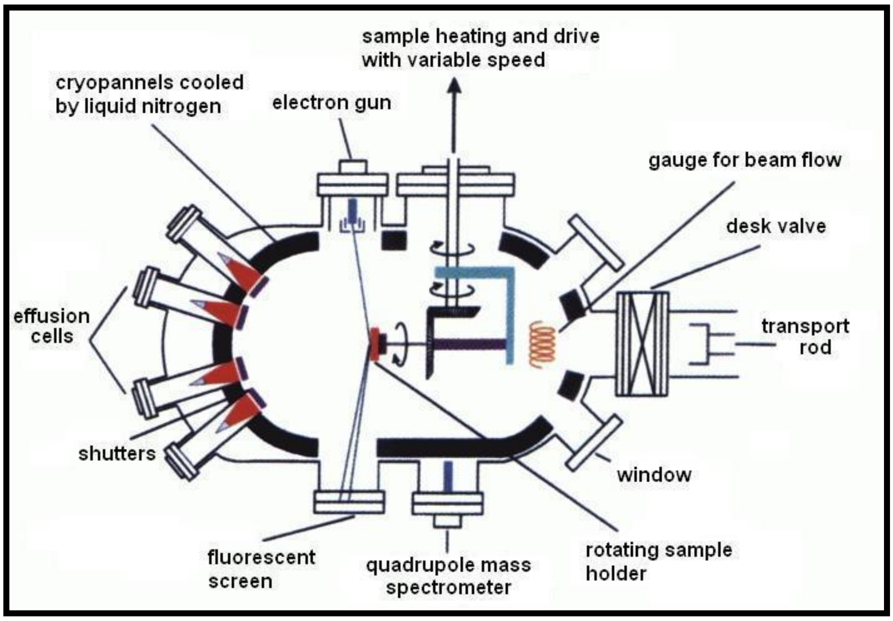
sample heating and drive with variable speed
cryopannels cooled by liquid nitrogen
electron gun
gauge for beam flow
desk valve
effusion cells
transport rod
shutters
window
fluorescent screen
quadrupole mass spectrometer
rotating sample holder

Fig.3.1: A schematic of Molecular Beam Epitaxy system.

The most advantageous aspect of MBE growth is the slow deposition rate (usually <500 nm/h) which enables the films to grow epitaxially. This has been possible through the use of effusion cells (Knudson cells), in which the group III-metal sources and dopants are placed in a crucible and heated until the material sublimates or evaporates. The temperature of the effusion cells is controlled by proportional-integral-derivative (PID) control parameters, where the flux intensity can be maintained to better than 1%. To introduce nitrogen, our system uses a nitrogen RF plasma source, where purified N_2 is converted into a more active atomic and molecular species. Shutters placed in front of the III-V sources permit direct control of the epitaxial growth surface at a monolayer level by changing the incoming beam with the opening and closing of the shutter. The GaN nanowall network studied in this work has been grown in Plasma Assistant Molecular Beam Epitaxy (PAMBE) system (SVTA Assoc. Inc., USA) which is shown in Fig. 3.2.

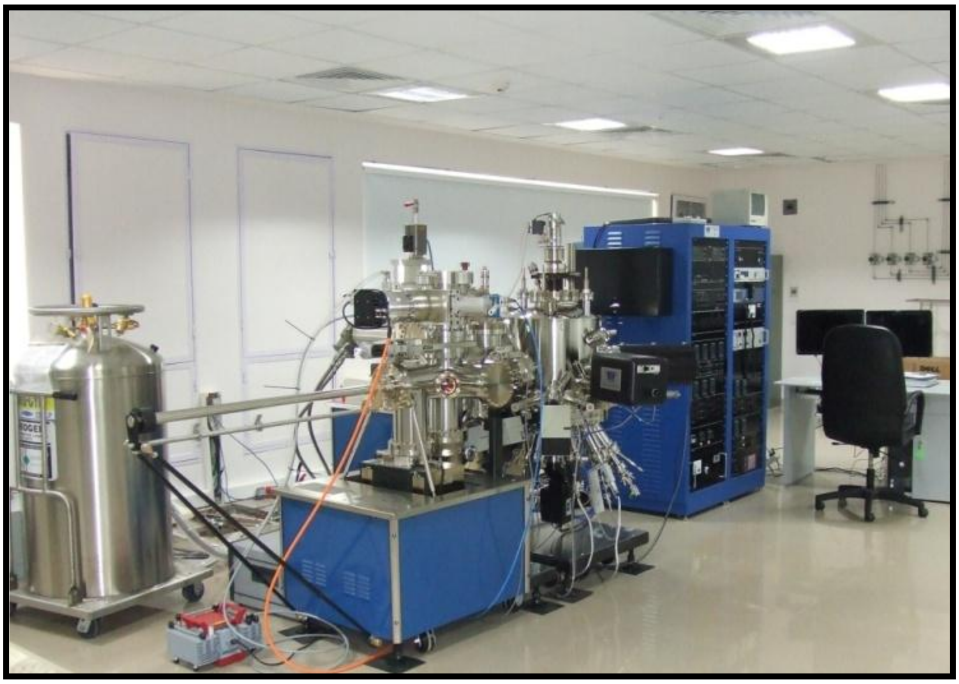

Fig. 3.2: SVTA MBE system used for growing GaN nanowall network.

2.2 Characterization tools

Different characterization techniques used in this work are:

1. SEM /FESEM
2. EDX/Elemental Mapping
3. XRD/HR-XRD
4. Atomic force microscopy (AFM)
5. Cathodoluminescence(CL) and Photoluminescence(PL)
6. Photoelectron Spectroscopy -XPS
7. Hall and I-V measurement - Van der Pauw method
8. Resistivity measurements – PPMS
9. Magnetic measurements - SQUID
10. Thermoelectric power measurements

2.2.1 Scanning electron microscope (SEM)

A scanning electron microscope (SEM) is a type of electron microscope that images a sample by scanning it with a beam of electrons in a raster scan pattern. By raster type scan pattern we mean that the beam sweeps horizontally left to right and keeps moving one step down after each scan. The secondary electrons that are produced by their interaction with the sample surface produce signals that contain information about the sample's surface topography, composition, and electronic structure etc. Areas ranging from approximately 1 cm to 5 microns in width can be imaged in a scanning mode using conventional SEM techniques (magnification ranging from 20X to approximately 30,000X, spatial resolution of 50 to 100 nm). The SEM is also capable of performing analyses of selected point locations on the sample; this approach is especially useful in qualitatively or semi-quantitatively determining chemical compositions (using Energy-dispersive X-ray spectroscopy (EDS or EDX)) [33].

An electron beam is thermionically emitted from an electron gun which is fitted with a tungsten filament as a cathode. There are other cathodes with low work function also available, such as lanthanum hexaboride (LaB_6), but tungsten is more commonly used because of its low cost, high melting point and low vapour pressure, the latter two properties enabling the electron emission to occur. The electron beams have energies between 0.5 to 40 keV, and are focused using two condenser lenses to a spot 0.4-5 nm in diameter. The beam passes through the scanning coils, which deflect the beam in x and y directions in order to get the raster effect during scanning. There are various types of electronic amplifiers which are used to amplify the signals which are displayed as variations in brightness on a cathode ray tube. The resultant image is a distribution of intensity of the signal being emitted from the scanned area of the specimen. The image is captured digitally and viewed on a computer screen [34].

Field Emission Scanning Electron Microscope (FESEM) is a modified Scanning Electron Microscopy technique with a modified electron source. The thermionic source (Tungsten/LaB_6) in a standard SEM apparatus is replaced by a Field Emission Source (Tungsten). The field emissive source works by applying an extremely large field on the cathode (~100nm) so that the electrons overcome the metal work function. The advantage of the field emissive source is the control over the energies of the emitted probing electrons. The energies of the source can be made very low and large in comparison to the thermionic source. This results in lower thermal drift, higher brightness contrast and lesser charging of the sample. This enables better resolution (1.5nm) and the possibility of imaging insulating samples efficiently. The FESEM images and EDX measurements were performed with a NOVA Nano SEM 600 from FEI, Netherlands.

2.2.2 Energy-dispersive X-ray spectroscopy (EDX), Elemental mapping

Energy-dispersive X-ray spectroscopy (EDS or EDX) is a very useful analytical technique used for the elemental analysis or chemical characterization of a sample. Interaction of an X-ray excitation source and sample are investigated owing to the principle that each element has a unique atomic structure that allows distinct signature peaks in its X-ray spectrum.EDS makes use of this unique signature obtained in X-ray spectrum emitted by a solid sample bombarded with a focused beam of electrons to obtain a localized chemical analysis. All elements from atomic number 4 (Be) to 92 (U) can be detected in principle, though not all instruments are equipped for 'light' elements ($Z < 10$). Qualitative analysis involves the identification of the lines in the spectrum and is fairly straightforward owing to the simplicity of X-ray spectra. Quantitative analysis (determination of the concentrations of the elements present) entails measuring line intensities for each element in the sample and for the same elements in calibration Standards of known composition. These measurements are performed in the SEM or FESEM setups, which are designed primarily for producing electron images, but can also be used for element mapping [35, 36].

2.2.3 Atomic Force Microscopy

The atomic force microscopy was invented in 1986 by Binning, Quate and Gerber. This Microscopy is one of the first techniques capable of measuring distances in fractions of a nanometer. The AFM for the first time made it possible to image with such a high precision all types of surfaces including insulating samples.

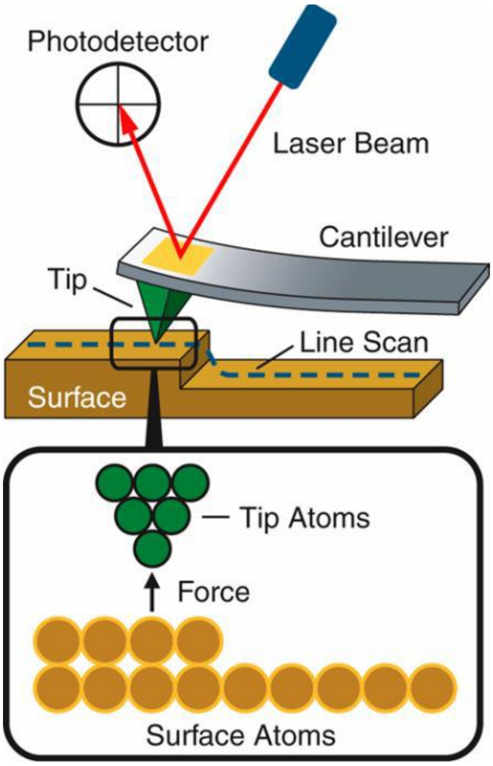

Fig.3.3 Principle of an AFM - laser beam is reflected from the back of the cantilever and is detected by a photodetector. The tip is extremely sharp with a single atom at the tip end

The AFM consists of a cantilever wherein a small tip is attached to a strip. The tip which regulates the precision of the AFM is a SiN/Si_3N_4 or Si tip micro-fabricated to have a radius of curvature in the order of a few nanometers or less. The Tip-Sample interaction causes the bending of the cantilever which is governed by the Hooke’s Laws. This displacement of the tip is typically measured by the change in the reflection spot of a laser incident on the cantilever. The movement of the reflection spot with the bending cantilever is monitored by a Differential Photo-diode detector array. Optical interferometry, Piezo-response and capacitive sensing are other alternatives to monitor the cantilever bend. There is a continuous feedback system where the deflection of the cantilever modulates the scanning parameters of the cantilever. The type of feedback is dependent on the mode the AFM is being operated in. The AFM is employed in many imaging modes- typically the Contact mode, Non-Contact mode and the Tapping Mode.

2.2.4 Magnetic Force Microscopy (MFM)

Magnetic Force Microscopy is a modified Atomic Force Microscopy where a fine magnetized tip (~nm) scans the sample instead of a standard tip. A standard AFM tip is coated with a ferromagnetic material with high coercivity such as Co. The sample-tip magnetic interaction is then quantified in a Dynamic AFM mode and mapped out in X-Y. The measurements are not as straightforward as AFM measurements as the tip magnetic field also effects the sample magnetization [35].

In our measurements an Interleave mode is used for imaging which is a line by line two pass technique. In first pass, the topography of the surface is scanned then in the second scan, the MFM tip is lifted to a prescribed height and either the phase or frequency variation of the tip from its resonance is monitored and projected as an image. This image is the measure of the long range forces experienced by the tip during scanning. These long range forces could be either coloumbic or magnetostatic. In the present study the Co tip is magnetized using a hard magnet. The typical values of coercivity and magnetic moment for the tip are 300 Oe and $4E^{-13}$ emu.

Magnetic force gradient causes shift in cantilever resonance frequency, given by

$$\frac{\Delta f_0}{f_0} = -\frac{\nabla F}{2k}$$

Co coated AFM tip measures the magneto-static forces between tip and sample,

$$\vec{F} = -\nabla E = \mu_0 \int \nabla\left(\vec{M}_{tip} \cdot \vec{H}_{sample}\right) dV_{tip}$$

The resulting dipolar probe – sample interaction can be expressed as

$$\delta\phi = \frac{\mu_0}{4\Pi} \frac{12\Pi Q}{k\left(\frac{d}{2} + R + c + s\right)^5} m_p m_s \frac{180}{\Pi}$$

where m_p and m_s is the magnetic moment of the tip and sample, Q is the quality factor of the tip in air ~ 150, k – spring constant, R radius of the tip ~ 70 nm, c thickness of chromium ~ 20 nm, d sample thickness and s – lift height.

Taking the value of m_p~ 2 X 10^{-12} Am^2 from the above reference, the calculated average m_s value is 2.5 X 10^{-18} Am^2. For the present calculations we took the whole sample thickness which is 860 nm where as the actual contribution for the MFM phase variation could be top few layers which constitutes a typical thickness ~ 30 nm.

2.2.5 Photoluminescence (PL) and Cathodoluminescence (CL)

Luminescence is the emission of light by a substance. It occurs when an electron returns to the electronic ground state from an excited state and loses its excess energy as a photon. Luminescence (both PL and CL) is an essential non-destructive analytical technique useful in a wide range of applications including semiconductors, optoelectronics, dielectrics and ceramics [35].

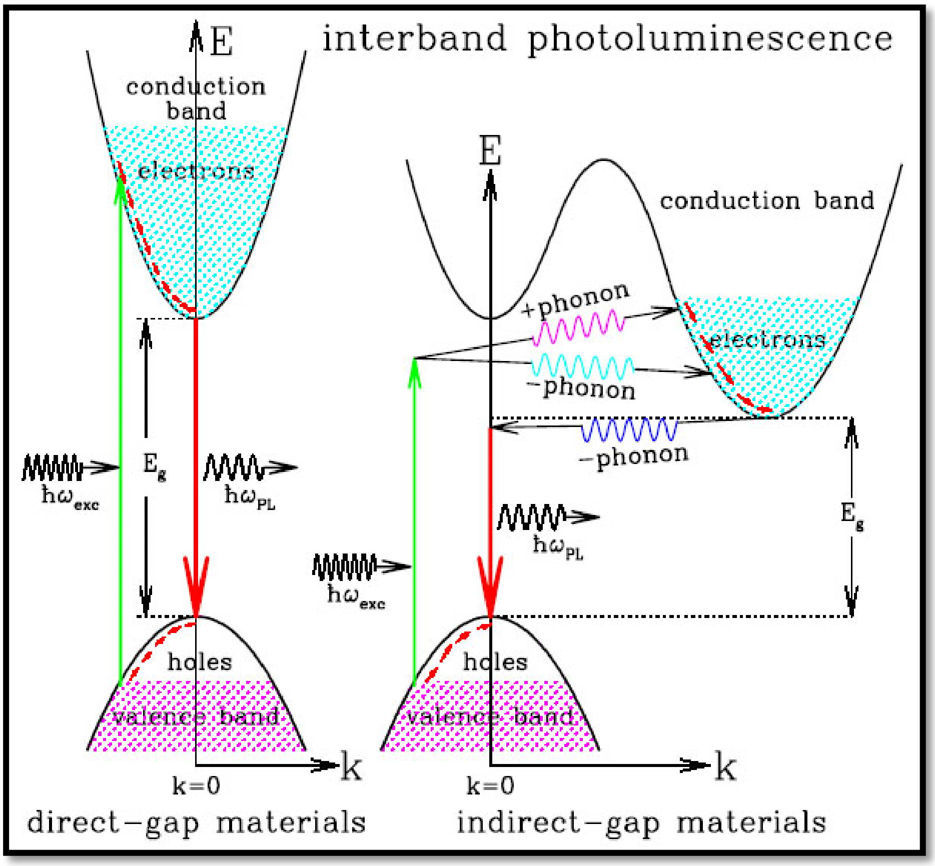
interband photoluminescence
E
conduction band
electrons
E_g
$\hbar\omega_{exc}$
$\hbar\omega_{PL}$
holes
valence band
k
k=0
direct−gap materials
E
conduction band
+phonon
electrons
−phonon
−phonon
$\hbar\omega_{PL}$
$\hbar\omega_{exc}$
E_g
holes
valence band
k
k=0
indirect−gap materials

Fig 3.4: Schematic band diagrams for the luminescence processes in a direct band gap (left) and an indirect band gap (right) material [37]

Photoluminescence (PL) is the process of absorption of photons by a material, which is then excited to a higher energy state and then returns to the lower energy ground state accompanied by the emission of a photon. The period between absorption and emission is typically extremely short, in the order of 10 nanoseconds. Time resolved Photoluminescence (TRPL) is another method, mostly used in the case of III-V semiconductors to measure the minority carrier lifetimes. The sample is excited with a light pulse and then the decay in photoluminescence with respect to time is measured.

Cathodoluminescence (CL) is similar to PL, differing only in the source of excitation. Here a high energy electron beam falls onto a semiconductor which results in the promotion of electrons from the valence band into the conduction band, leaving behind a hole. When an electron and a hole recombine, a photon is emitted.

2.2.6 Van der Pauw method - Hall and I-V characteristics

This is the most commonly used method to do Hall and I-V measurements, accurately measures the properties of a sample of any arbitrary shape, that is approximately two-dimensional (i.e. thickness << width) and whose electrodes are placed on its perimeter. From the measurements made, various properties of the material like resistivity, majority carrier type, sheet charge density and mobility of the majority carrier can be calculated. This method is particularly useful for measuring very small samples because effects due to a sample's size, which is the approximate probe spacing, are irrelevant.

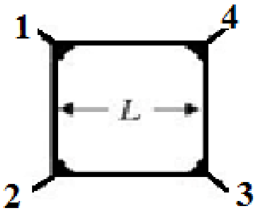

Fig. 3.5: Contact geometry for the Van der Pauw method.

To make a measurement, a current is caused to flow along one edge of the sample (for instance, I_{12}) and the voltage across the opposite edge (in this case, V_{34}) is measured. From these two values, a resistance (for this example**,** $R_{12,34}$) can be found using Ohm's law:

$$R_{12,34} = \frac{V_{34}}{I_{12}}$$

Van der Pauw showed that, for a flat two dimensional body of arbitrary shape, the sheet resistance R_s satisfies

$$\exp\left(-\pi R_{12,34}/R_s\right) + \exp(-\pi R_{23,41}/\mathrm{R_s}) = 1$$

which allows the sheet resistance to be determined from simple electrical measurements. Reciprocity theorem gives,

$R_{12,34} = R_{34,12} = R_{21,43} = R_{43,21}$

Averaging these we can get a much more accurate measure of the sheet resistance, cancelling out any offset voltages. Similarly accurate values of the Hall voltage can also be determined, for example I_{24}, in the presence of either a positive or negative magnetic field, and a Hall voltage is measured between the other two corners, for example $V_{13}^{\pm}$, where ± denotes the polarity of the magnetic field. The average Hall voltage is then given from

$$V_H = \frac{V_{13}^{+} - V_{13}^{-} + V_{24}^{+} - V_{24}^{-} + V_{31}^{+} - V_{31}^{-} + V_{42}^{+} - V_{42}^{-}}{8}$$

Hence the accurate values for the sheet carrier density and mobility of the sample can be measured using each set of currents and voltages for the Hall voltage and sheet resistance measurements.

We performed Hall measurements using Ecopia HMS-2000 Hall effect measurement system. Indium contacts are made to the sample in the Van der Pauw geometry and Ohmic nature of the contacts is shown by linear I-V curve. This system has a 0.58 T permanent magnet, and the polarity of the field is changed by rotating the magnet by 180^0. A current upto 20 mA can be passed by the system and if required, low temperature measurements at 77 K can be performed by filling the sample holding container with liquid nitrogen.

2.2.7 Powder X-ray Diffraction

X-ray diffraction is a powerful, non-contact method used in order to understand the crystalline phases in bulk materials, thin films and powder samples. Additionally, X–ray diffraction can determine the strain state, grain size, epitaxy, phase composition, preferred orientation, and defect structure of individual phases. X-ray diffraction is based on constructive interference of monochromatic X-rays and a crystalline sample. A cathode ray tube (CRT) is used to generate X-rays, which are then filtered to produce monochromatic radiation, collimated to concentrate and then directed towards the sample. If the wavelength of the incident radiation matches the diffraction angle and the lattice spacing (d_{hkl}), then as per Bragg's law constructive interference takes place and a diffracted ray is emitted.

$$2\mathbf{d}_{hkl}\sin\theta = n\lambda$$

Here d_{hkl} is the spacing for a hkl plane, θ is the glancing angle, n the order of diffraction and λ the wavelength of x-ray used (1.54 Å for CuKα).

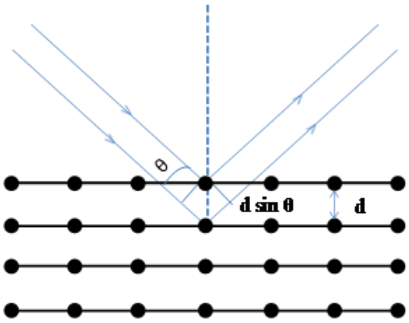

Fig.3.6: Schematic showing diffraction of x-rays from Bragg planes at a grazing angle θ.

Many diffracted rays are collected by scanning the sample through a range of 2θ angles and counted. Thus, for quantitative phase determination both peak position as well as peak intensity needs to be crucially analyzed. Phase purity of the sample is usually analyzed by comparing the observed experimental pattern against the database maintained by International Centre for Diffraction Data (ICDD).There are primarily three types of diffraction techniques based on X-rays: a) Single crystal X-ray diffraction, 2) Powder diffraction, and 3) High- resolution X-ray diffraction.

High-Resolution XRD (HR-XRD) is mostly used to determine the properties of thin epitaxial films. Many methods that make HRXRD useful for studying epitaxial films are – rocking curves, ω-2θ coupled scans, reciprocal space maps and reflectivity scans. Major advantage of HR-XRD over a conventional XRD is the amount of resolution it provides in the pattern, which may go up to as sharp as 10 arc-secs. Rocking curves are measured by fixing the incident angle (ω), and varying the reflected angle (2θ). If a peak does not occur when the reflected angle matches the incident angle, then the sample is not mounted properly. Flatness of the sample surface can also be analyzed by using the rocking curve.

X-ray diffraction patterns of the samples were recorded with a Bruker D8 Advance X-ray diffractometer using a Cu Kα x-ray source to confirm the phase purity.

2.2.8 X-ray Photoelectron Spectroscopy

X-ray photoelectron spectroscopy (XPS), also known as Electron Spectroscopy for Chemical Analysis (ESCA), is the most widely used surface analysis technique because of its relative simplicity in use and data interpretation. It was first designed by by K. Siegbahn and his research group at the University of Uppsala, Sweden in the mid 1960s and since then it has been extensively used to study the chemical composition and oxidation state at the sample surface.

It is based on the photoelectric effect discovered by Einstein in 1905. Principle of Photoemission states that if an atom absorbs a photon, an electron from the core shell of the atom will be ejected out, provided that the photon energy is greater than the sum of that electron binding energy (E_B) and the work function (Φ) between Fermi level (E_f) and Vacuum level (E_v) as shown in Fig. The zero binding energy position is defined as the

Fermi level (E_f). Hence, applying the principle of conservation of energy, we get the resultant kinetic energy, E_K, possessed by the photoelectron as:

$$E_K = h\nu - E_B - \Phi.$$

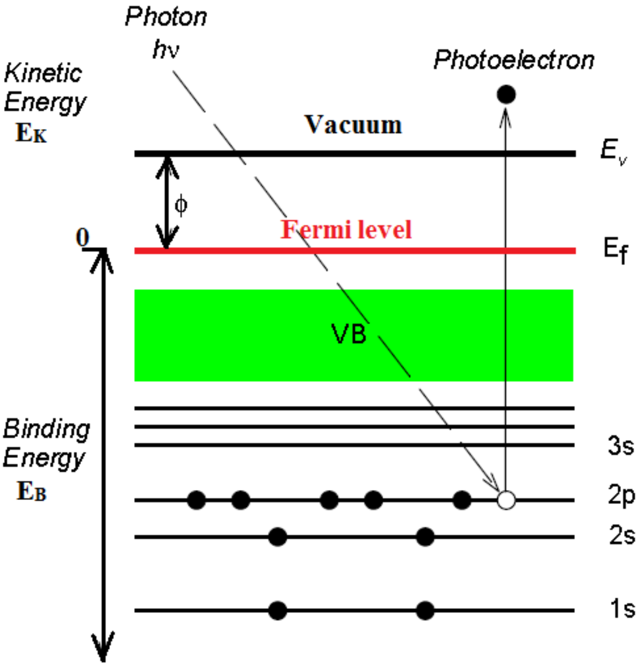

Fig.3.7: Principle of Photoemission.

Changing to binding energy we get,

$$E_B = h\nu - E_K - \Phi.$$

Here, if $h\nu$ and Φ are known, the measured E_K would allow us to obtain the E_B. Since each element has unique set of core levels, hence the outgoing electrons would vary in their kinetic energies. This gives a characteristic peak for each element in the XPS spectrum and can be used to identify elements.

XPS is able to detect most of the elements except hydrogen and helium, because of their low sensitivities. Normally Al or Mg are used as an anode material for the X ray source since most of the core levels are in the 0-1000eV range. The most intense lines are called $K_{\alpha 1}$ and $K_{\alpha 2}$, but often the doublet is viewed as one line and called $K_{\alpha 12}$. It has energy of 1253.6 eV and 1486.6 eV, for Al and Mg, respectively. Typically a hemispherical analyzer, which acts as a band-pass filter, is used for the collection of the photoelectrons in XPS. It consists of two con-centric hemispheres held at different potentials. Only those electrons that have kinetic energy higher than the pass energy E_p can pass the analyzer. An electrostatic lens-system can be placed in front of the hemispheres in order to focus the electrons into the analyzer and to change the angular acceptance. Fig 3.8 shows a schematic of the standard XPS system [36].

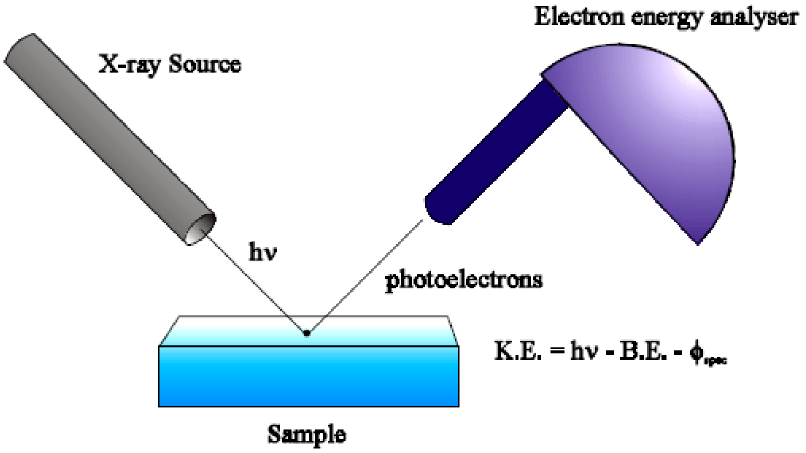

Fig. 3.8: Schematic of XPS system

.

XPS measurements given in the present work are carried out using Omicron SPHERA analyzer with non monochromatic X-rays viz. Mg-Kα (hν = 1256.6eV) and Al-Kα (hν = 1486.6eV) and the deconvolution is achieved using the standard software with a curve-fitting mathematical process based on a Voight profile which is implemented in Fityk , an opens source package.

2.2.9 Magnetic Measurements: SQUID Magnetometer

Different magnetometers are available for studying magnetic materials. A SQUID (superconducting quantum interference device) is a very sensitive magnetometer used to detect incredibly small magnetic fields , based on superconducting loops containing Josephson junctions. SQUID consists of two superconductors separated by thin insulating layers to form two parallel Josephson junctions. SQUIDs are sensitive enough to measure fields as low as 5 aT (5×10−18 T) within a few days of averaged measurements. Since flux associated with a Josephson junction is quantized in units, the great sensitivity of the SQUID devices is associated with measuring changes in magnetic field associated with one flux quantum given by

$$\boldsymbol{\Phi_0 = \frac{2\pi\hbar}{2e} = 2.0678x10^{-15} tesla.m^2}$$

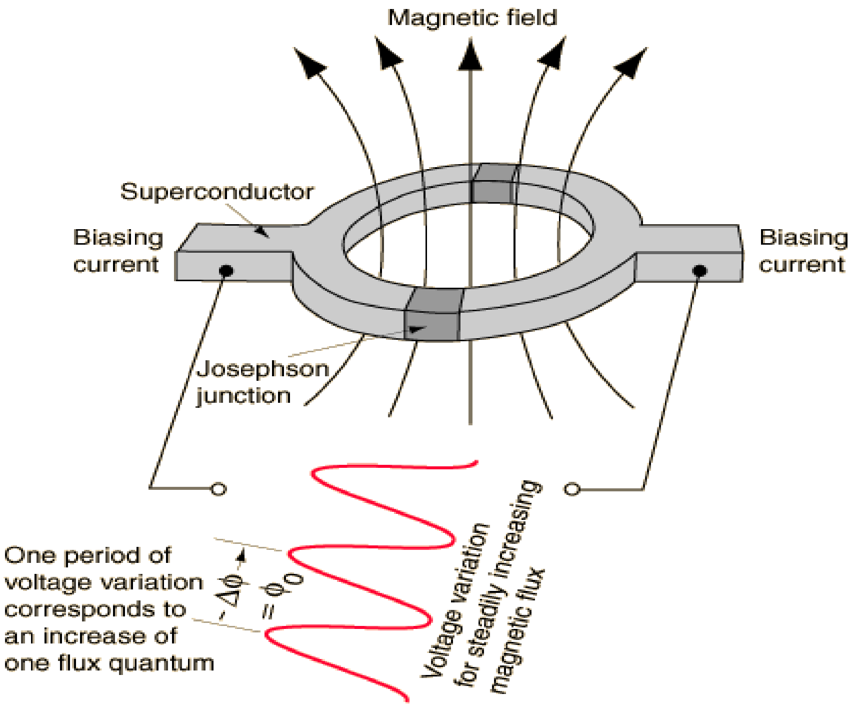
Magnetic field
Superconductor
Biasing current
Biasing current
Josephson junction
One period of voltage variation corresponds to an increase of one flux quantum
Δφ = φ0
Voltage variation for steadily increasing magnetic flux

Fig3.9: Operating principle of SQUID.

If a constant biasing current is maintained in the SQUID device, the measured voltage oscillates with the changes in phase at the two junctions, which depends upon the change in the magnetic flux. Counting the oscillations allows us to evaluate the flux change which has occurred.

Fig 3.10: SQUID used for the magnetic studies in the present work, Quantum Design, Inc.

Magnetic studies in thesis are carried out by using a superconducting quantum interference device of Quantum Design, USA. Temperature dependence of Field-cooled (FC) magnetization, in the ranges of temperature (T) from 5 K up to 300 K is measured by cooling the sample to low temperature in the presence of magnetic field (10 Oe) and data were collected on heating the sample. M-H curves were recorded at various temperatures with magnetic field (H) varying from 0 T to 0.5 T.

2.2.10 Thermo power measurements

We have designed a simple and handy setup to do the thermo power measurements on the various GaN nanostructured thin films. Fig 3.11 shows a schematic of the setup. It consists of two copper blocks that hold the sample in between and act as hot and cold sink. A heater consisting of high resitance coil wrapped around mica sheets is embedded inside one of the copper block to act as the hot end. Two thermocouples are attached to the sample to measure the temperature of hot and cold ends respectively. The two ends of the sample are also connected to a digital multimeter by chromel-alumel thermocouple that reads the voltage generated as a function of the temperature difference. Standard n and p type Si samples were used to standardise the system and later on measurements on GaN network and epilayer were performed.

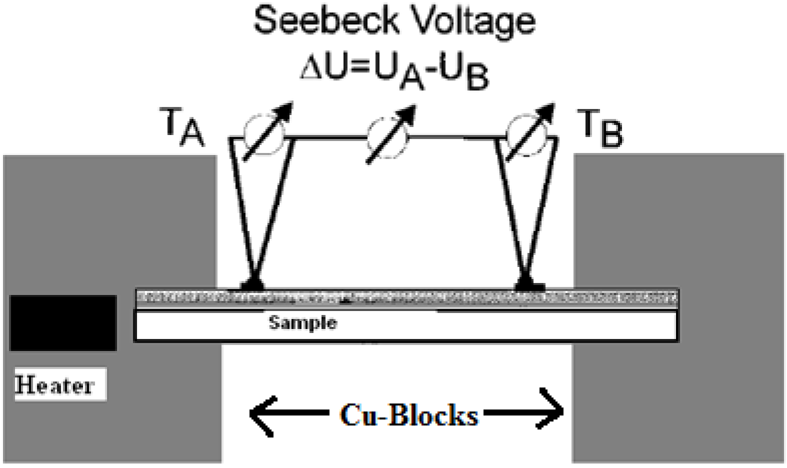
Seebeck Voltage
$\Delta U = U_A - U_B$
T_A
T_B
Sample
Heater
Cu-Blocks

Fig3.11: Homemade setup to measure thermo emf as a function of temperature.

Chapter 3

Results and Discussion

Chapter - 3

Results and Discussion

Properties of the GaN nanowall network

The GaN thin film with nanowall-network morphology studied in this thesis was grown in plasma assisted molecular beam epitaxy (PA-MBE) system (SVTA, USA) with a base pressure of 2 x 10^{-10} Torr. The c-plane sapphire substrate was chemically cleaned and thoroughly degassed in vacuum to ensure atomic cleanness, as seen by the characteristic reflection high electron energy diffraction (RHEED).

Effusion cell held at 1000°C provides the Ga molecular beam onto a rotating 3 inch Al_2O_3 c-plane substrate and a 375W RF nitrogen plasma at a working pressure of 2.5 x10^{-5} Torr was used to nitride the incoming Ga flux. The conditions at which this interesting nanowall network was obtained are: Ga Beam equivalent pressure (BEP) of 2.3 x10^{-7} Torr, substrate temperature of 680°C and Nitrogen flux rate of 4.5sscm. Under this nitrogen rich condition, Ga adatoms diffuse over short distances before they get nitrided, promoting 3D nucleation at the steps of edge dislocations and the strain relaxes to form a hexagonal GaN nanowall network, surrounding a void region which consists of open screw dislocations [31, 32].

In situ RHEED patterns recorded along the $[11\bar{2}0]$ azimuth were used to monitor the growth and it was seen that the distance between RHEED spots in these characteristic transmission patterns through nanostructures in lateral and vertical direction is 1.89 which is equal to $2a^*/(\sqrt{3}c^*)$ ratio ($a^* = {}^{2\pi}/_{a}$ and $c^* = {}^{2\pi}/_{c}$) , implying that the c/a ratio is1.63 confirming the c-oriented wurtzite structures of these nanowalls. Fig 3.1 shows one such RHEED pattern obtained. The anisotropy in these spots is indicative of the nanowalls, as will be discussed later [31].

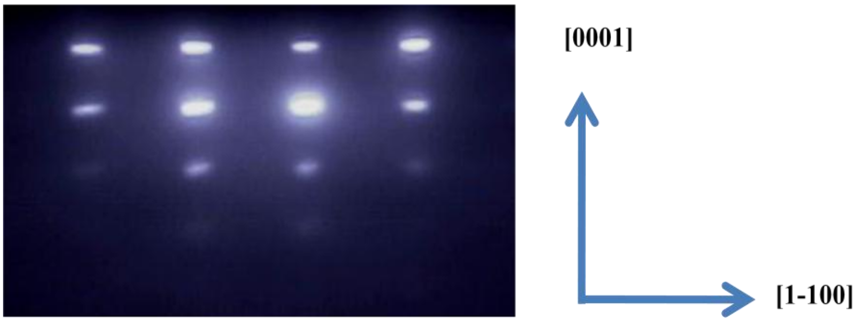

Fig 3.1: RHEED pattern of the GaN film grown on c-plane sapphire along $[11\bar{2}0]$ *azimuth*

Post growth conventional ex-situ material characterization by FESEM, XRD and PL were done to examine the purity of material. The photoluminescence spectra showed a high intensity band edge emission at ≈3.5eV, with a negligible defect band in the proximity of ≈ 2.2eV fairly well in keeping with the literature values for GaN films. XRD pattern of the film confirms the fact that the gallium nitride film was single crystalline and wurtzite in nature and oriented along c-axis. FESEM images showed a hexagonal tri-branched network like morphology.

A second look at these conventional characterizations showed that though the films were pure and highly crystalline but the FWHM of PL band edge and XRD peaks were unusual. It was seen that the walls were about 150 nm at the bottom, which tapered down to 10 nm at their apex. This further motivated us to do an in-depth study of the properties of this nanowall network and probe their dependence on this morphology, which led to further characterizations of electronic structure, electrical, magnetic and thermal transport properties using AFM, MFM, SQUID and I V-Hall measurements etc.

This chapter presents a detailed analysis of the various properties of nanowall network compared with a 2-D flat TDI, MOVPE grown 2μm thick GaN epilayer.

3.1 FESEM and EDX (elemental mapping)

To look at the morphology of the films, a FESEM micrograph was acquired which showed a network like morphology. Plan and tilted view images were taken and it was seen that the network is made up of wedge shaped GaN nanowalls that are about ≈ 150 nm thick at the bottom and taper down to ≈10-20 nm at the apex and are oriented in-planes along $[11\bar{2}0]$ and $[11\bar{1}0]$ crystallographic directions. (Fig 3.2 and 3.3)

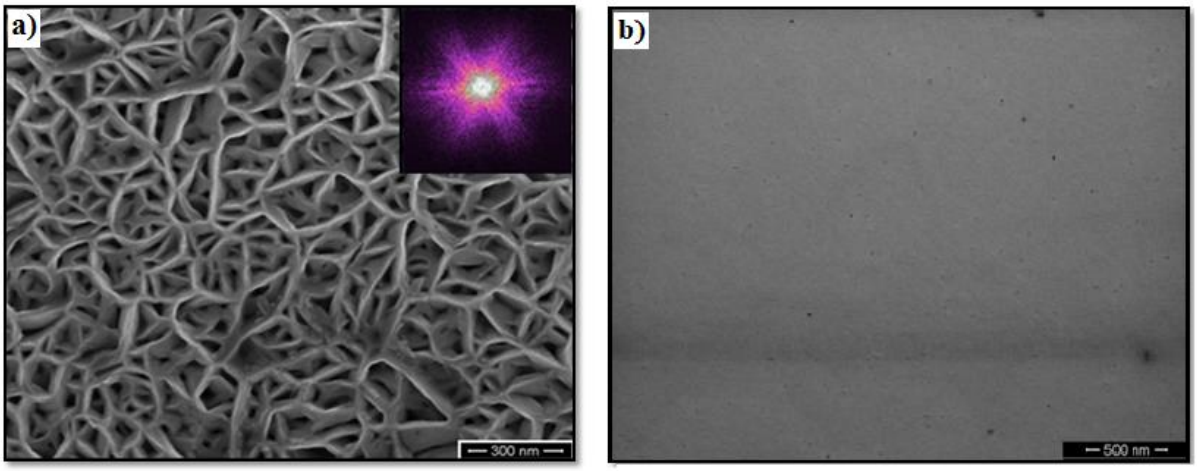

Fig 3.2: FESEM image of a) GaN nanowall-network, b) GaN- Epilayer and inset shows FFT for the same image

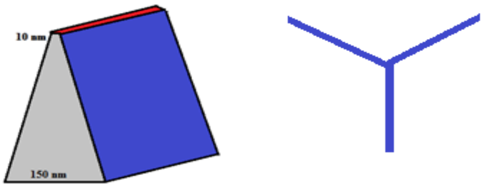

Fig 3.3 Wedge shaped morphology of the network contributes a huge surface area (left) and a tri branch (right) a typical feature of the network.

It was also noticed that the network structure grows as larger hexagons incorporating the smaller ones. These walls circumscribe micro-cavities (voids) having an areal density ~ $10^9/cm^2$, which coincides with the aerial density of extended defects in a typical MBE GaN film, suggesting that that the voids can be open screw dislocations.

Further FFT analysis performed on the FESEM image (using MATLAB) shows that nanowall network has a 6-fold symmetry (inset of fig 3.2). FFT has a bright spot in the centre suggesting long range order in this morphology. Whereas for the GaN epilayer we did not see any such features. FESEM image shows morphology of the surface with dark pits as a signature of threading dislocations.

Compositional analysis was done for both GaN epilayer and nanowall network utilizing the Energy Dispersive X-ray (EDX) attached to the FESEM system (from *Brϋker)*. This instrument has a resolution of 0.129 eV. The EDX analysis produced information from depth and XPS is used to analyze the surface composition of the films. It is seen that Nitrogen to Gallium ratio was close to 1 for the epilayer, while the nanowall network had a dearth of nitrogen, which can be attributed to background nitrogen vacancies [38]. Fig 3.4 shows a quantitative picture of the elemental compositions of both epilayer and the nanowall-network, obtained from the EDX measurements. It is well established in literature that GaN films are naturally nitrogen deficient due to less solubility of Nitrogen in the lattice at typical growth temperatures [38].

In GaN the defect with the overall lowest formation energy is the nitrogen vacancy, under both Ga-rich and N-rich conditions [1]. If deviations from stoichiometry occur due to point-defect formation, they will therefore always tend toward nitrogen-deficient material (even under N-rich conditions). This was confirmed by explicit self-consistent calculations of point-defect concentrations and stoichiometries by Van de Walle *et. al* [38, 39]. The reason for this asymmetry in GaN can be found in the high binding energy of nitrogen molecules, which makes it difficult (or even impossible) for the GaN solid to ever become nitrogen-rich: Nitrogen atoms much prefer to leave the solid and become part of N_2 molecules, rather than incorporate in the solid in the form of nitrogen-rich point defects [39].

The EDX spectra for nanowall network showed very trace amounts of Carbon and oxygen as well. (Not shown here). This could be due to surface impurities incorporated while exposing the samples to environment.

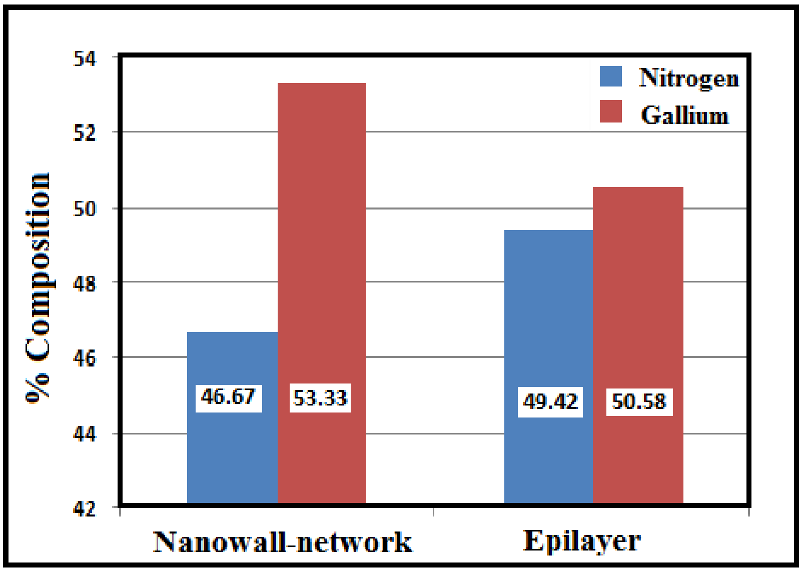

Fig3.4: Bar graph showing relative composition of GaN epilayer and nanowall-network as measured by EDX spectra (with reference to standard GaN sample)

3.2 XPS measurement

To know the surface composition of the nanowall network XPS measurements were acquired and peaks corresponding to major elements Gallium, Nitrogen, Oxygen and Carbon were observed. All the spectra were corrected for the shift during measurements by taking C-1s peak as reference. Percentage composition of the elements present on surface was calculated taking into account the relative Atomic Sensitivity factors for the analyzer in the given geometry. Fig 3.5 shows the XPS spectra for the GaN nanowall network and percentage composition of various elements present on the surface. Apart from Ga and N, oxygen and Carbon contamination was also observed. This C contamination can be due to handling of samples in open air, whereas sources of oxygen impurities need not be the same. This showed that the surface was also N-deficient, supporting the previously obtained EDX spectra. Due to handling the sample in air, carbon contamination was detected on the film,. It was possible to get rid of the contamination via energetic 2keV Ar^+ ion sputtering (spectrum not shown here), and then it was confirmed that the GaN films were clean, while the contaminants were only on the surface due to sample handling.

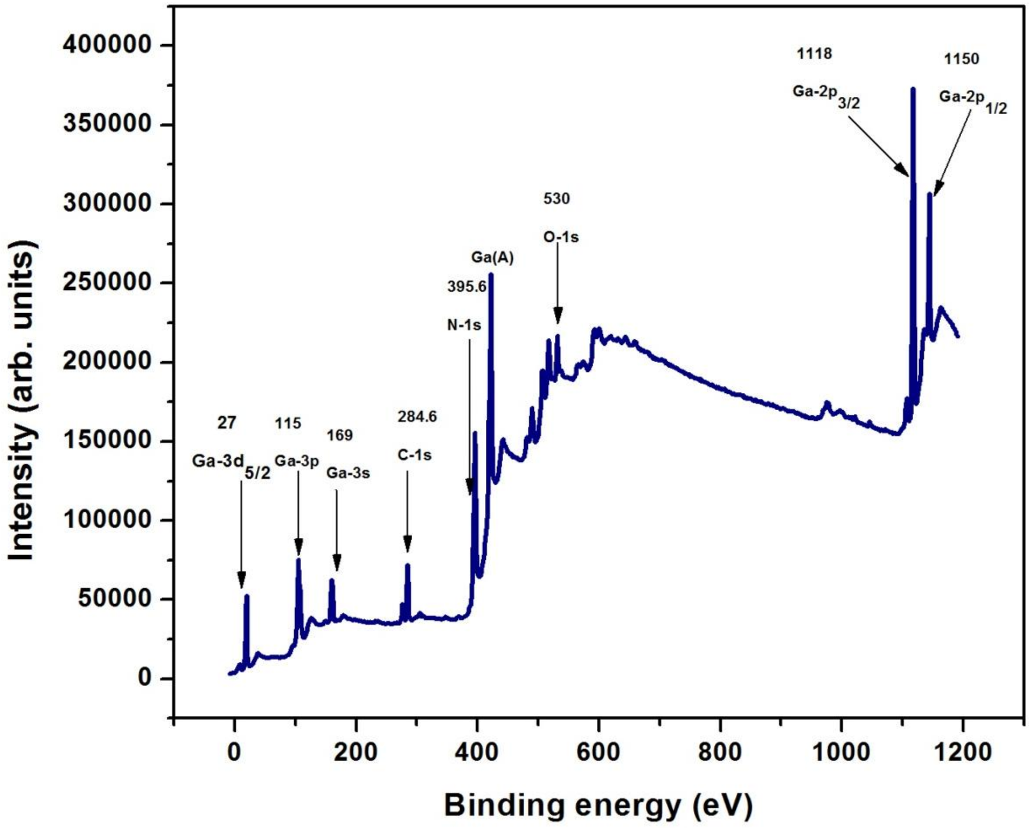

Fig.3.5: XPS spectra of GaN nanowall network grown on sapphire (0001) plane

At this point, to further examine the crystalline quality and structure of the GaN nanowall network we progressed to XRD measurements.

3.3 XRD-HRXRD measurements

To determine crystalline quality and probe into the structural properties of the GaN nanowall network the X ray diffraction pattern was recorded by a high-resolution x-ray diffractometer (*HRXRD from Bruker, Germany*) with a resolution of 50 arc sec. The orientation of the epitaxial films was determined by X-ray diffraction, and the crystalline quality was investigated by generating rocking curve along (0002) reflection. The XRD pattern for the GaN nanowall network is shown in the Fig 3.6.

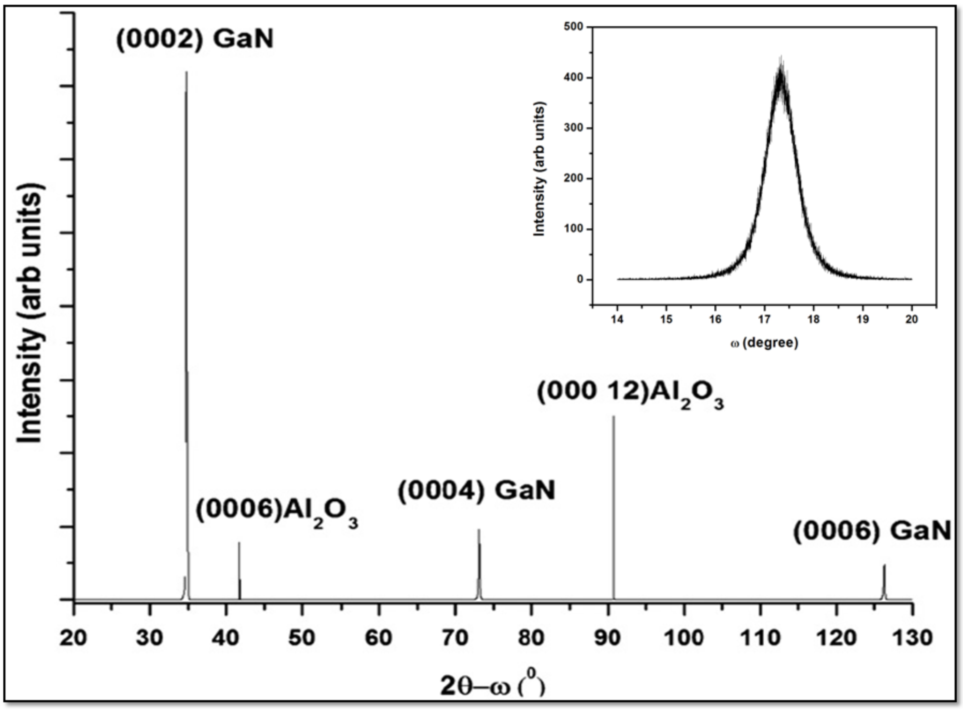

Fig. 3.6: HRXRD scan of the GaN nanowall network, inset shows the rocking curve measured at (0002) reflection for GaN nanowall network

Prior to XRD measurements, sample alignment was done at 2θ = 41.68° which corresponds to the peak position of (0006) reflection from Al_2O_3 substrate, with a probable error in measurements ≈ 0.03°. Due to diffraction geometry of θ-2θ diffractometer, the only diffraction event detected arises from the crystal planes parallel to the substrate surface. The XRD Peaks at 2θ = 34.54° and 72.8° are due to reflections from (0002) and (0004) plane, respectively, of wurtzite GaN. Therefore we conclude that the GaN nanowall network grows with its c plane parallel to the c-plane of the substrate surface. No additional peaks in XRD patterns confirm that the films are single crystalline and single phase.

A closer look at the FWHM (≈ 900 arc secs) of the peaks in 2θ-ω pattern is an indicative of the crystalline quality of the material. The full-width at half- maximum (FWHM) of the rocking curve measured at (0002) reflection for GaN nanowall network was found to be 2000 arc sec (inset of fig 3.6). These FWHM values are indicative of a mosaic and crystalline material [1]. To further explain this we looked at the size effects arising due to nano dimension of the system.

While broadening in the (0002) symmetric reflection of GaN is generally attributed to the mosaicity or tilt in the columnar features [40], broadening of FWHM of XRD peaks (2θ-ω pattern) can be explained by the famous Debye – Scherrer formula [41] that says

$$\beta = K\lambda/(Dcos\theta) \quad \ldots\ldots\ldots\ldots\ldots\ldots\ldots\ldots \quad (3.\ 1)$$

where,

D – is the size of crystallites.

K – is the Debye constant

λ =1.54056 Å is the wavelength of the X-ray radiation

β is the peak full width at half maximum in radians, and

θ is the Bragg diffraction angle for the (0002) reflection for GaN nanowall network

We know that the nanowalls taper from 150 nm at the bottom to 10 nm at the apex; hence the FWHM of their XRD peaks is expected to show the following behaviour as a function of width of the walls, as depicted by fig. 3.7.

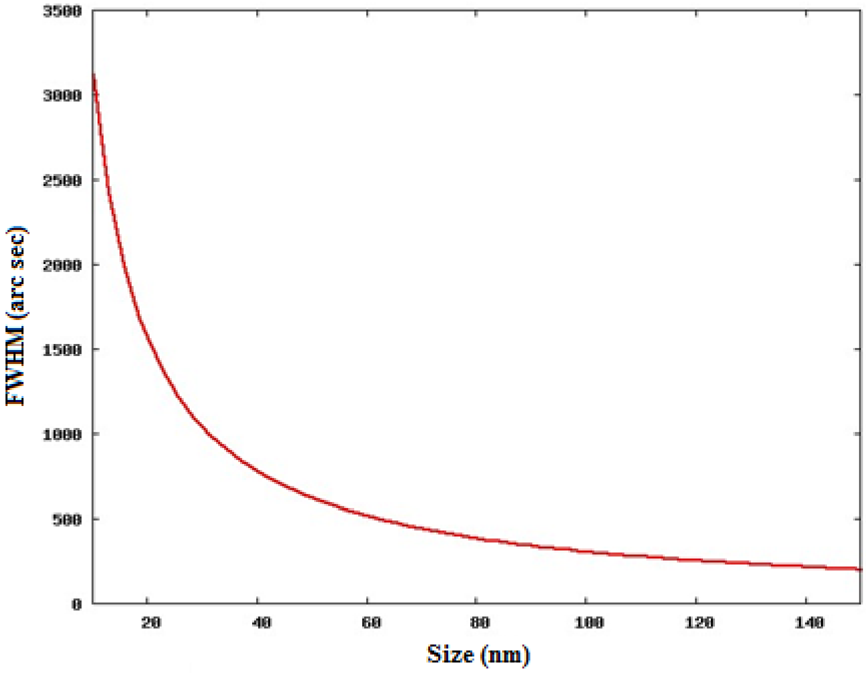

Fig. 3.7 Dependence of FWHM of rocking curve on Size of the crystallites (As determined by the Debye-Scherrer relation)

For high quality GaN thin films previously Mustukas *et. al.* have reported the FWHM of the peaks to be approximately 50 arc secs. These small values of FWHM indicated small variations in interplanar spacing along the c-axis. They attributed the observation of extensive broadening in some other samples to a high density of edge threading dislocations [40].

So, for the case of GaN nanowall network thin film the observed broadening may be due to a continuous variation of size (perpendicular to c axis) and the tilt in these walls with respect to the c axis that may result in closely spaced peaks for each set of interplanar distance and angle. These two factors Debye Scherre broadening and the angle of walls with respect to the c axis are expected to be responsible for the broad FWHM ≈ 900 arc secs for 2θ-ω pattern and ≈ 2000 arc secs, of rocking curves around the (0002) reflection for GaN nanowall network. These characterizations clearly showed that the size effects are playing an important role here and they might further result in properties that are completely unexpected of bulk GaN.

3.4 Characterization of Band Edge emission: CL spectra

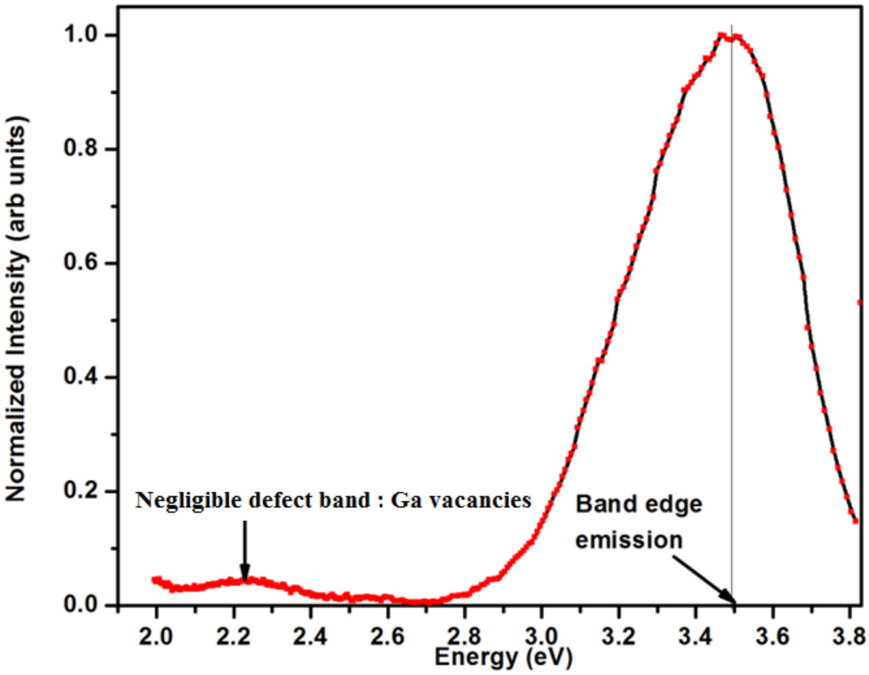

Fig3.8: CL spectra of GaN nanowall network showing the band edge emission at 3.5eV and the 2.2 eV defect band which is attributed to the Ga vacancies present in the system

To look at the emission properties of the nanowall network, cathodoluminescence spectra was taken at 300 K and it showed band edge emission associated with GaN in the proximity of 3.45 eV and this along with previous measurements confirmed that the GaN network was made up of pure, single phase and highly oriented single crystalline GaN crystallites. A negligible defect band was seen at 2.2 eV, which is generally attributed to the defect states, in particular Ga vacancies [1] present in the system (Fig 3.8). Absence of defect associated peak confirms the high optical quality of GaN nanowall network (Fig 3.9). Typically FWHM of band edge emission associated with GaN thin films is approximately ≈ 50 – 90 meV [40, 42]. But, in case of thin film with GaN nanowall network the FWHM of associated band edge emission was ≈ 600meV even though defect emission was not observed. This raised our curiosity and we progressed to further detailed Photoluminescence studies to examine the root of such wide emission.

3.5 Detailed Photoluminescence Analysis

Photoluminescence (PL) spectroscopy has been the workhorse of the optical characterization techniques due to its non-destructive nature and ability to yield valuable information about both intrinsic and extrinsic transitions. The latter is important since both defect-related and near bandgap transitions are frequently observed in GaN. Photoluminescence measurements have become particularly useful in the last decade when unintentionally doped GaN with a background n-type carrier concentration in the low 10^{16} cm^2 has become available. One can resolve the closely placed near bandgap exciton-related PL lines using low temperature measurements.

3.5.1 Literature background

Two typical photoluminescence spectra of high quality unintentionally doped GaN grown by HVPE and measured at room temperature and at 6 K (Fig. 3.9[42]). As seen in Fig. 3.9, the PL spectrum changes drastically when going from 300 to 6 K. The most apparent differences are the temperature dependence of the optical bandgap energy and the thermal broadening. At 6 K (solid line), well-resolved PL peaks appear near the intrinsic optical bandgap energy. The strongest peak at 3.473 eV is attributed to bound exciton recombination. More specifically, this exciton recombination is associated with a neutral donor (D^0X), since unintentionally doped GaN invariably is n-type. The bound excitons are typically observed up to approximately 100 K, where the bound excitons thermally dissociate, leaving the free exciton recombination to dominate the spectrum [43]. Thus, the main PL peak observed at room temperature (broken line) at 3.404 eV is attributed free A-exciton recombination, but the fine structure is not resolved at room temperature due to thermal broadening.

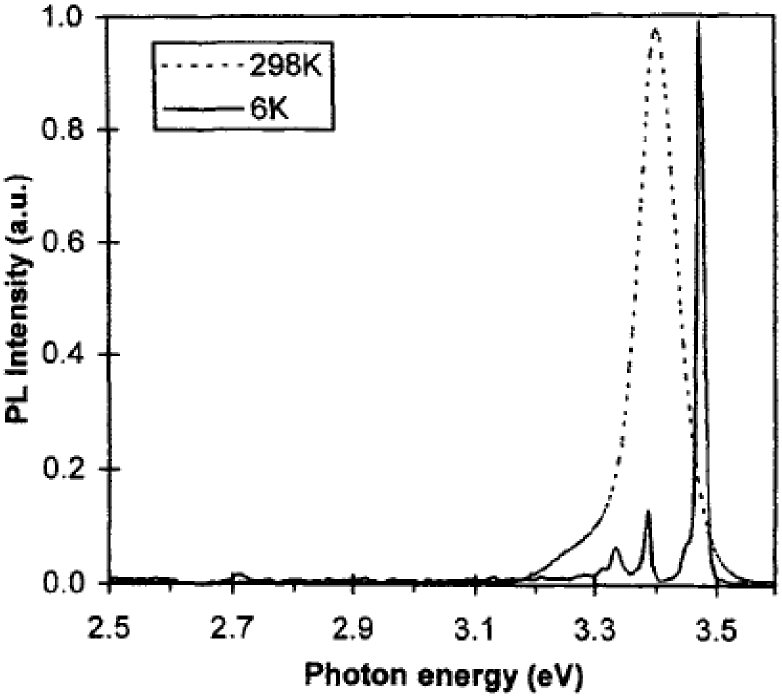

Fig.3.9. Photoluminescence spectra of unintentionally doped GaN measured at room temperature (broken line) and at 6 K (solid line). (adapted from [42]*)*

The binding energy of the free A-exciton has been extracted from Arrhenius plots of the PL intensity at approximately 27 meV , compared to a value of about 26 meV extracted from a comparison with the spectral location of the A-exciton's excited (n = 2) state . The free excitons binding energy measurement places the lowest bandgap energy at ≈ 3.504 eV at 2 K. Furthermore, the donor-bound exciton binding energy is approximately 6 meV, as determined by measuring the energy difference between the bound and free excitons (n = l) lines [44-50].

The most frequently observed defect-related luminescence is the often referred to as the 'yellow band' due to the spectral location at about 2.2 eV. The origin of the yellow luminescence has been attributed to transitions of free (or weakly bound) electrons from the conductions band edge (or a shallow donor level) to a deep acceptor level located about 860 meV above the valence band edge [51]. This theory was later supported by pressure-dependent PL measurements [52]. It was further suggested that the acceptor level is due to gallium-vacancies [51]. Recently, theoretical investigations have provided support for the gallium-vacancy theory and suggested the shallow donor level is associated with oxygen [53]. Further support for the gallium-vacancy involvement in the defect-related PL is provided by experiments demonstrating that the yellow PL can be suppressed in GaN grown under gallium-rich conditions.

It is important to note that the exact spectral location of the exciton peaks strongly depends on the residual strain in the GaN layer, and can vary several tens of meV depending on growth and substrate [42].

3.5.2 PL for nanowall network

Photoluminescence (PL) measurements performed on the nanowall network were compared with a thin film GaN sample taken as reference sample (Fig 3.10(a)). A blue shift of ~78 meV of the band edge peak was observed. This shift may be a consequence of the residual strain or quantum confinement effects at the thinner regions of the nanowalls in this network like morphology. Due to large lattice mismatch at the GaN/Al_2O_3 interface, this nanowall network morphology seems to be a consequence of the strain relaxation and we expect to see a fingerprint of such process in the PL spectra.

Moreover the full width at half maxima (FWHM) of the nanowall sample (290 meV) was found to be much higher than that of GaN thin film reference sample (80 meV). To probe further into nature of this broad band edge emission we performed a temperature dependent study of the PL emission. It was seen that the PL intensity increased as the temperature was lowered. Contrary to what is expected, there was no effect on the FWHM and it nearly remained same. Even at temperatures as low as 10 K, no excitons related peaks could be resolved. Hence, we conclude that this broadening of the band edge peak is not a lattice (phonon) related phenomenon, rather it might be purely an electronic phenomenon which is being enhanced by the morphology of this network structure (resulting in cavity photonics).

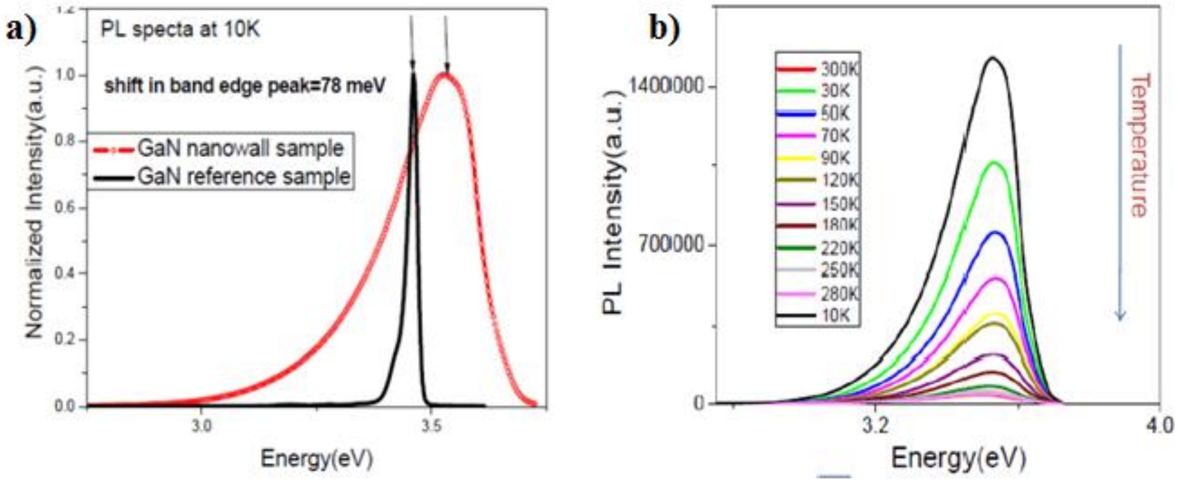

Fig. 3.10: a) PL spectra taken at 10K for the GaN nanowall network and GaN reference sample, and b) Temperature dependent PL study of the GaN nanowall network

Variation of integrated PL intensity as a function of temperature was studied for the GaN nanowall-network sample and the thin film reference sample. The exciton binding energy is found to be higher for the case of network (36 meV) than for the GaN thin film reference (28 meV). This increase in exciton binding energy could again be a possible indicative of quantum confinement [54]. This exciton binding energy when studied as a function of temperature shows a slow decrease for the nanowall network sample which indicates that the electron-phonon coupling is clearly less in the GaN nanowall sample, which can again be a possible signature of quantum confinement.

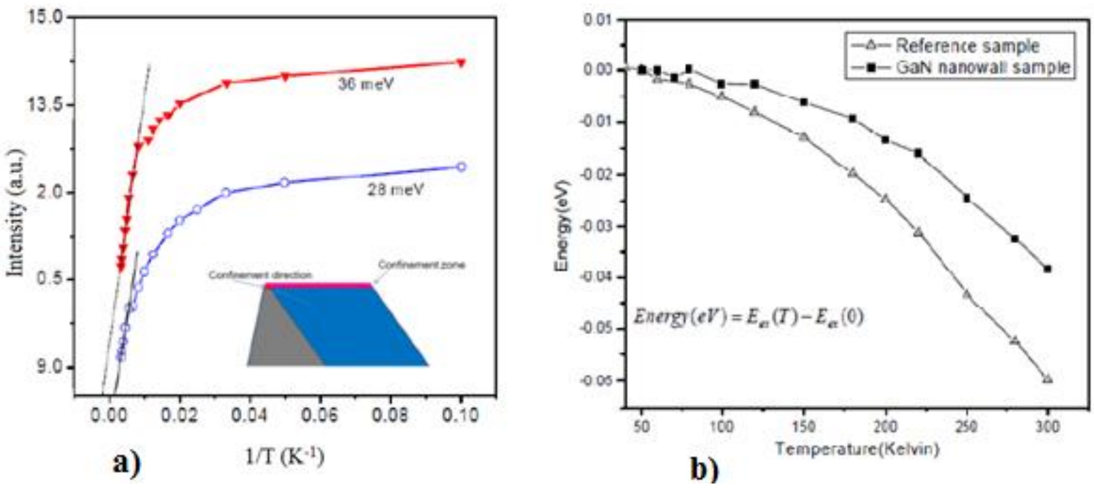

Fig. 3.11: a) Integrated Pl intensity Vs inverse temperature and b) Temperature dependence of exciton energy

The temperature dependence of the bandgap in semiconductors is often described by an empirical expression (assuming no localization),

$$E(T) = E(0) - {\alpha T^2}/{(\beta + T)} \tag{3.1}$$

where, α (in units of energy over temperature) and β (in units of temperature) are material constants.

In case of localization, which can be construed as band tail effect, the temperature dependence deviates from the above equation. In the framework of band tail model and Gaussian-like distribution of the density of states for the conduction and valence band, the temperature-dependent emission energy could be described by the following modified expression[54], which is based on a model developed for Stokes shift in GaAs/AlGaAs quantum wells [55].

$$E(T) = E(0) - \left[{\alpha T^2}/{(\beta + T)} \right] - \left[{\sigma^2}/{(kT)} \right] \qquad (3.2)$$

where, the last term represents the localization component with σ indicating the extent of localization or band tailing, which is nearly imperative for GaN films with high carrier concentration.

This GaN nanowall network films has very high background carrier concentration (~ 10^{20}/cm^3 details in later section on hall measurement), which is similar to an unintentional doping of n type carriers in the system due to N vacancies. It has been reported in literature that as doping increases PL peak blueshifts due to band filling and FWHM can increase due to thicker band of states from which transition can be made and as the temperature is lowered the Intensity also increases by enhancing the probability of radiative recombination [42]. So we suspect that due to high carrier concentration there might be transitions to higher energy states (higher than CBM) which could possibly lead to formation of a large density of band tail states in the nanowall sample.

This broad band edge emission which remains coherent even at low temperatures could be very useful in emission devices. Hence, in order to map the emission from these nanowall samples and study the effect of network like morphology on the characteristic emission from GaN (resulting in cavity photonics), we performed CL mapping for further investigations, since CL has high spatial resolution.

3.6 Cathodoluminescence (CL): CL Spectra and CL imaging

3.6 .1 Motivation and Literature background

Trapping light in a small modal volume enables the storage of optical power at specific resonant frequencies. This is useful in a large number of fields such as cavity QEDs, photonics, biosensing and nonlinear optics. Optical microresonators have led the way in the structural aspects of such devices and many devices based on Fabry-Perot cavities, photonic crystals and whispering gallery modes (WGMs) have been fabricated worldwide.

III-V structures have gained much importance in this field due to their excellent luminescent properties. It has been seen that III-V Quantum Dots (QD) placed inside a III-V microcavity can efficiently capture and confine electrons and holes [56-58]. ZnO nanowall network has been suggested to show interesting microcavity effects [59]. Motivated by this we explore the GaN nanowall network structures as microcavities and probe the emission from them. Owing to the large FWHM observed in the PL and CL spectra we decided to probe the nature of this wide FWHM by using CL mapping spectroscopy as an imaging tool.

3.6 .2 CL mapping for nanowall network

SEM image and panchromatic CL map was acquired at room temperature (fig. 3.12). It was evident from the SEM images of the nanowall network that there is a large distribution of cavity sizes (diameters). CL mapping on this nanowall matrix showed that the band edge emission of GaN is focused and emitted out of the cavities in the network. It was also noticed that not all the cavities emit, and the intensities also differ slightly.

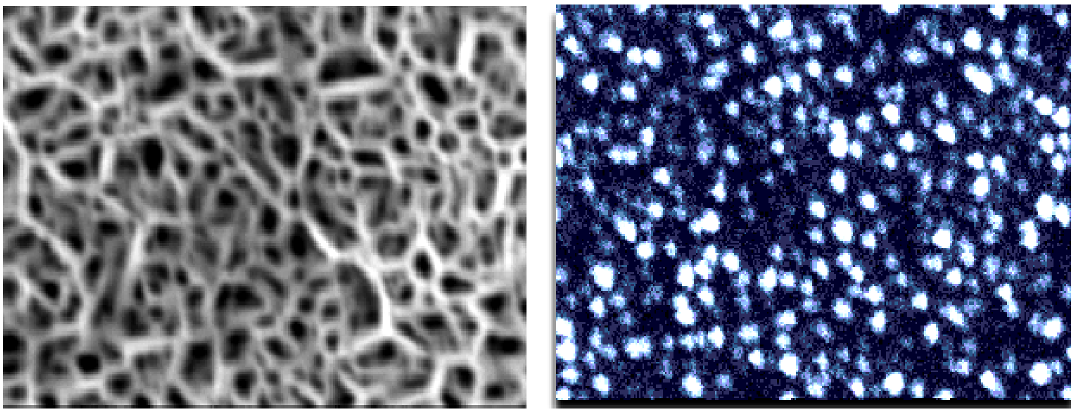

Fig 3.12: SEM micrograph of the nanowall network (left) and CL imaging showing the emission centers (right)

Size distribution of the cavities and the emission spot size was plotted (fig. 3.13) and the most probable diameter for the cavities as well as the emission spot was found to be ≈ 180 nm. Fig 3.13 shows the distribution in cavity and emission sizes and a Gaussian fit for the same. It is clearly evident from the fig. 3.13, that though there is a large distribution in the dimensions of cavity sizes (FWHM of Gaussian fit ~ 120 nm), they emit with approximately the same emission spot size (FWHM of Gaussian fit ~ 36 nm) , like a coherent emission.

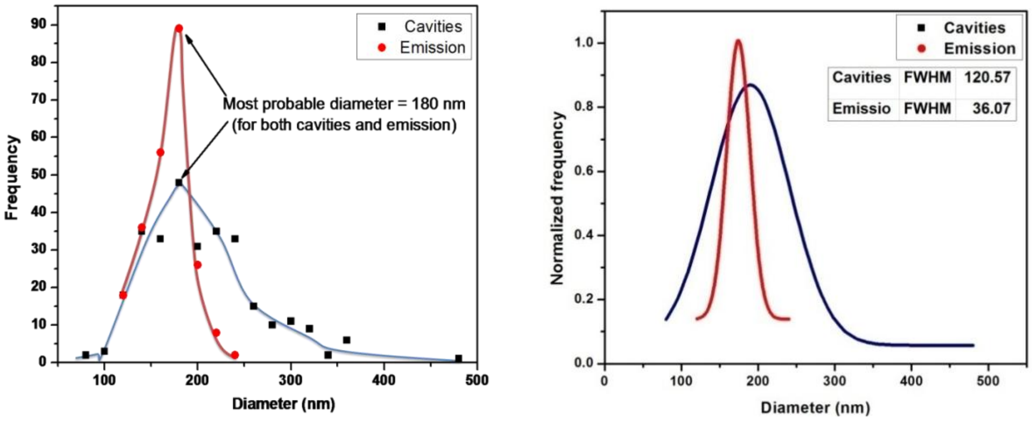

Fig.3.13: Distribution of cavity and emission sizes (left) and a Gaussian fit for the size distribution (right).

Investigations to understand the nature of this emission are under progress. There are reports on Whispering gallery modes in ZnO nanowall network [59, 60]. To understand our observations in light of Whispering Gallery Modes like phenomenon, we selected a bright emission and the corresponding cavity and performed line scans using ImageJ.

Fig 3.14 shows the averaged line scan wherein we can clearly see that the maxima of emitted light lies at the center of the cavity, whereas in a whispering gallery type cavity the maxima of intensity must lie skirting the periphery with no intensity being observed at the center of the cavity. Hence, in our case this argument of a whispering Gallery like phenomenon is less probable and we explore the possibility of Fabry-Perot like cavities.

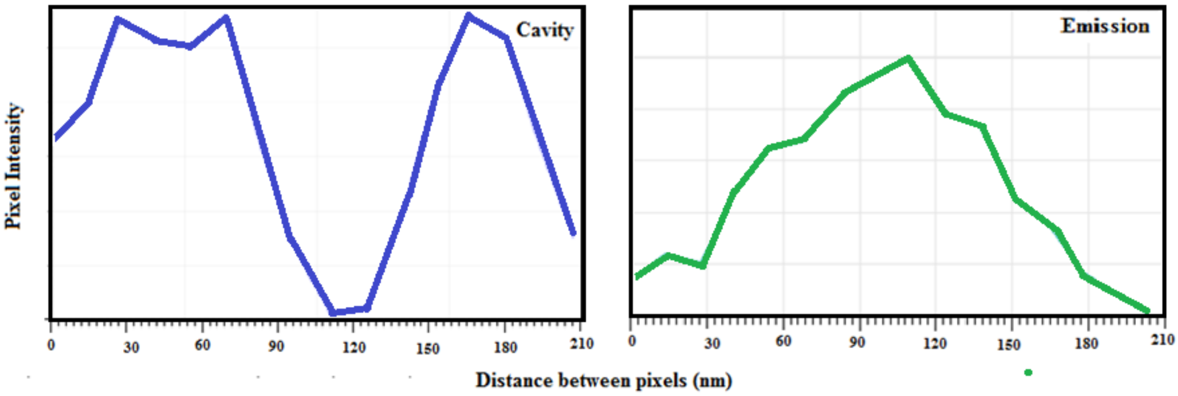

Fig. 3.14: Line profile across the cavity and corresponding emission (using ImageJ)

To understand these curious results, we explored the possibilities of modes present in the Fabry-Perot cavities. Fabry-Perot style resonators consist of two highly reflecting mirrors which provide with a feedback mechanism. In an analogy to that fact, we propose that the GaN nanowalls (Fig. 3.15(a)), which emit the band edge emission, can be treated as highly reflecting mirrors (Fig. 3.15(b)). The narrowness of the top of the walls further aids in focusing the emission and the resultant spot size that is seen is spherical and extremely intense.

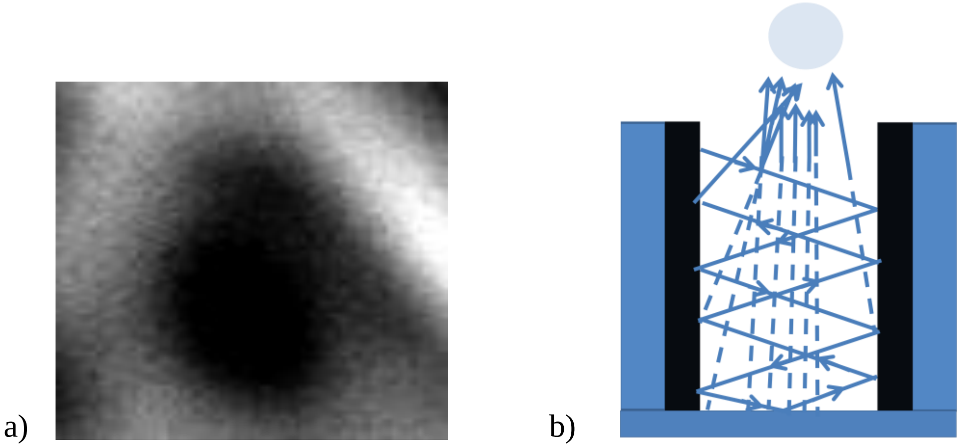

Fig. 3.15: a) A typical cavity seen in the nanowall network matrix. b) Possible geometry of emission considering a Fabry-Perot like geometry

Since all these measurements so far indicated presence of some sort of interesting electronic properties, we decided to look into the electrical transport properties of this nanowall network sample.

3.7 Hall and I-V measurements

Hall measurements were carried out in the standard Van der Pauw geometry. Indium contacts were made on the films for ease of operation. Ohmic nature of the contacts was established by plotting the I-V curves prior to hall measurements. Following table 3.1 presents a summary of the Hall measurements performed at 77 K and 300 K for GaN epilayer and Nanowall network samples.

Properties	**GaN- Epilayer**		**GaN – Nanowall network**	
	T = 300 K	**T = 77 K**	**T = 300 K**	**T = 77 K**
Volume carrier Concentration (N_B) [/cm^3]	-1.526E+18	-1.524E+18	-1.356E+20	-1.347E+20
Sheet Concentration (N_S) [/cm^2]	-3.051E+14	-3.047E+14	-1.085E+16	-1.078E+16
Mobility (μ) [cm^2/Vs]	7.737E+01	6.603E+01	1.694E+01	1.704E+01
Conductivity (σ) [1/Ω cm]	1.891E+01	1.612E+01	3.681E+02	3.679E+02
Resistivity (ρ) [Ω cm]	5.288E-02	6.205E-02	2.717E-03	2.718E-03
Average Hall Coefficient (R_H) [cm^3/C]	-4.092E+00	-4.097E+00	-4.603E-02	-4.633E-02
Magneto resistance at 0.5 T (δ) [Ω]	1.187E+00	1.188E+00	3.337E-02	3.359E-02

Table 3.1: Summary of Hall measurements

It is observed that both GaN epilayer and nanowall network showed a negative Hall coefficient, indicating that the majority carriers are electrons and nanowall network shows carrier concentrations ~ 10^{20}/cm^3, and low mobility. This low mobility can be understood keeping in mind the morphology of our nanowalls, which encircle giant dislocations [1].

Over the years, as-grown GaN samples are known to be *n*-type semiconductors without intentional doping, implying the presence of donors. These donors must be associated with defects or impurities, since perfect GaN cannot provide thermal carriers. This has been thought to be caused by the spontaneous formation of nitrogen vacancies. In GaN the defect with the overall lowest formation energy is the nitrogen vacancy, under both Ga-rich and N-rich conditions. If deviations from stoichiometry occur due to point-defect formation, they will therefore always tend toward nitrogen-deficient material (even under N-rich conditions) [38, 39]. This was confirmed by explicit self-consistent calculations of point-defect concentrations and stoichiometries. The reason for this asymmetry in GaN can be found in the high binding energy of nitrogen molecules, which makes it difficult (or even impossible) for the GaN solid to ever become nitrogen-rich: Nitrogen atoms much prefer to leave the solid and become part of N_2 molecules, rather than incorporate in the solid in the form of nitrogen-rich point defects [39].

When the material shows n type conductivity, it facilitates the formation of Ga vacancies in the system [42]. Moreover, existing reports on GaN thin films have shown that the Ga vacancy concentration correlates with the intensity of the yellow luminescence at 2.2 eV, suggesting that the acceptor states of V_{Ga} are involved in this optical transition. The YL was also found to be stronger in samples grown under N-stable conditions in MBE consistent with higher V_{Ga} concentrations when the growth is more N-rich. Hence, detailed information about the nature of vacancies present in our system can further need to be deconvoulted by a rigorous analysis of Photoluminescence (PL) and transport measurements.

Presence of Ga vacancies has lead the way to magnetism in undoped GaN films [61-65] and hence to explore the presence of Ga vacancies further we decided to do some magnetic measurements on our sample.

3.8 Magnetic Measurements

3.8 .1 Background

Diluted magnetic semiconductors (DMSs) have been extensively investigated due to their potential applications in spintronic devices which exploit both the spin and charge degree of freedom of carriers (electron/ holes) [61-71, 73-74]. Various doped and undoped II-VI and III-V systems have been explored for possibility of such applications. One such widely studied system is (Ga,Mn)N which has been reported to exhibit ferromagnetism with curie temperature (T_c) varying from liquid helium temperature to 940 K [73], depending on the relative concentration of the cations. But, a major drawback of making DMS materials is the low solubility of magnetic elements in the semiconductor compounds. However, if we can tailor the structural properties at nanoscale so as to get ferromagnetism without transition metal doping, this could be a significant advance for spintronics.

Over the years, reports have confirmed the observation of room temperature ferromagnetism in various thin films of nonmagnetic oxides (d^0 systems) viz. HfO_2, TiO_2, ZnO, and MgO and related materials [62-69]. The origin of ferromagnetism in such material has been long debated and sometimes attributed to the oxygen vacancies. Room temperature ferromagnetism observed by Sundaresan et.al. in GaN nanoparticles with different sizes, was attributed to the defects confined to the surface of the nanoparticles [62-64]. Recently, room temperature ferromagnetism has been postulated as a universal characteristic of nanomaterials of ZnO,Al_2O_3, MgO, GaN and CdS which are diamagnetic in bulk form [64]. This has been attributed to the fact that point defects in insulators can create localized electronic levels within the band gap that can have different electron occupancies and thus different charge states and magnetic moment [64]. But, this theory has been surrounded by controversies due to limitations in material synthesis which may result in accidental inclusion of ferromagnetic impurities or uncontrolled contamination from the surroundings or sample handling [65- 69, 75]. Theoretical investigations involving first-principles calculations have shown that Ga vacancies are responsible for the observed magnetism in GaN nanostructures. The magnetic moments mainly come from the unpaired $2p$ electrons at nearest-neighbour N atoms of the Ga vacancy. The defect formation energy at the surface is significantly different from that of the bulk due to structural and electronic effects [61]. A recent report by Basanta Roul et.al. has shown an experimental evidence for the manifestation of Ga vacancy induced ferromagnetism in GaN thin films [62]. Albeit, there is incessant investigation in this direction, the complete understanding about the origin of ferromagnetism in otherwise nonmagnetic semiconductors is such as GaN is still an open question.

The presence of the anomalous or Extraordinary Hall Effect (EHE) has been widely used to verify whether the system is a single-phase system magnetically. The EHE is due to spin polarization of carriers and spin-orbit coupling which can be caused by the magnetization of the material itself. Published works on (In,Mn)As, (Ga,Mn)As, and Mn:Ge have shown such a response in support of other characterization data showing the material to be single phase from a magnetic viewpoint [76]. Electrical transport measurements as a function of temperature and applied field have been used to probe detailed information regarding the magnetic ordering in Mn-doped GaN [74, 77]. The Hall resistance in ferromagnetic materials can be expressed by

$$R_{Hall} = R_0(B/d) + R_s(M/d) \tag{3.3}$$

Where, R_0 is the ordinary Hall coefficient, R_S is the anomalous Hall coefficient, d is sample thickness, and M the magnetization of the film.

Presence of EHE is also reflected in the temperature dependence of sheet resistance (R_{sheet}) at zero applied field, which was used to identify the Curie temperature in the (Ga,Mn)N samples by M. L. Reed et. al where the temperatures were varied from liquid nitrogen up to 380 K. Fig. 3.16 (adopted from [73]) shows anomalous Hall effect data (left) at 323 K and the temperature dependence of sheet resistance at zero applied field for two different Mn-diffused samples and an undoped GaN control sample (right) The Curie temperature was found to be in the range 220–370 K, depending on the diffusion conditions. For the same sample, fig. 3.17(adapted from [73]) shows the temperature dependence of the magnetization which was extrapolated using mean-field approximation to yield an estimated T_C of 940 K.

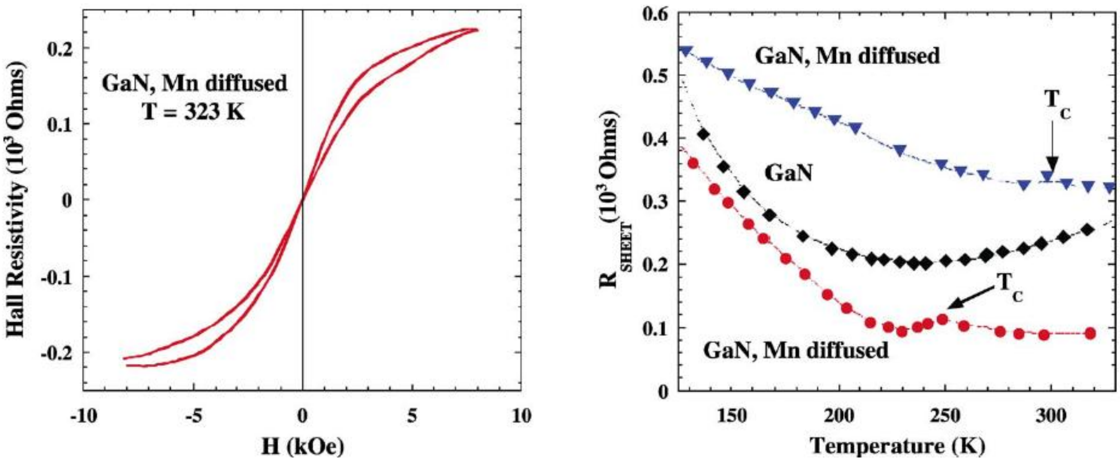

Fig.3.16: Temperature dependence of sheet resistance at zero magnetic field for Mn-diffused GaN and as-grown GaN (left) and room temperature anomalous Hall effect hysteresis curves for Mn-diffused GaN (right) (adapted from [73])

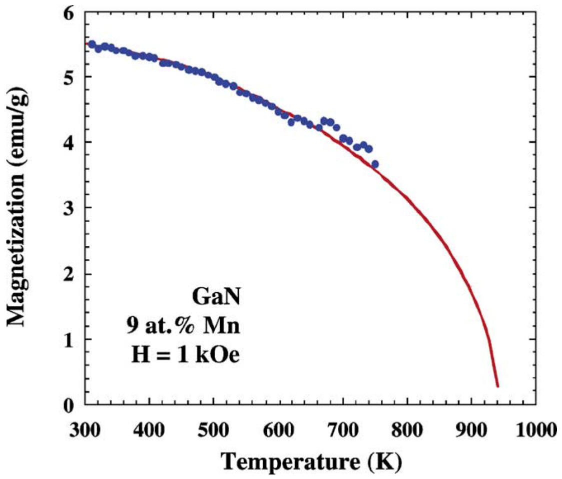

Fig. 3.17. Magnetization vs. temperature for (Ga, Mn)N sample grown by MBE with 9 at.% Mn. The extrapolation of the curve is based on a mean-field approximation (adapted from [73]*)*

The GaN nanowall network with tailored cavity sizes has the potential for a spintronics material as it contains large surface area with varying curvature and coordination. Hence, this can be representative of an important class of GaN based nano-structured building blocks for miniaturized electronic and optical devices. A fundamental understanding of the electronic and magnetic properties of these low dimensional ferromagnetic (FM) semiconductor nanostructures is crucial for the development of spintronics devices. This study aims at understanding magnetic properties for the GaN-nanowall network by I-V Hall, electrical and magnetization measurements presented. The presence of ferromagnetism has been supported with magnetic force microscopy (MFM) measurements and observation of Anomalous/Extraordinary Hall Effect (EHE) by studying the variation of sheet resistance as a function of temperature.

3.8 .2 Results

Recent controversies about the nanoscale magnetism in otherwise non magnetic materials, which has sometimes been credited as a purely surface phenomenon by some [62-64] and related to defects or impurities by others [65-69], raised our curiosity to perform magnetic measurements on this nanowall network which has a huge surface area and is grown under UHV conditions to discuss magnetism in GaN at nanoscale.

The GaN epilayer (~ 2μm thick), a representative of bulk GaN was found to be diamagnetic at all temperatures. This conforms to previous reports that state GaN is diamagnetic in bulk form.

The M-H curve for the GaN nanowall network at 2 K, before and after the strong diamagnetic correction for the sapphire substrate was employed, shows that hysteresis occurs with a saturation field of 4 kOe. The saturated magnetization is estimated to be $106\text{x}10^{-4}$ emu/cm^3 with coercivity 50 Oe and remnant magnetization of approximately $7\text{x}10^{-4}$emu/cm^3.

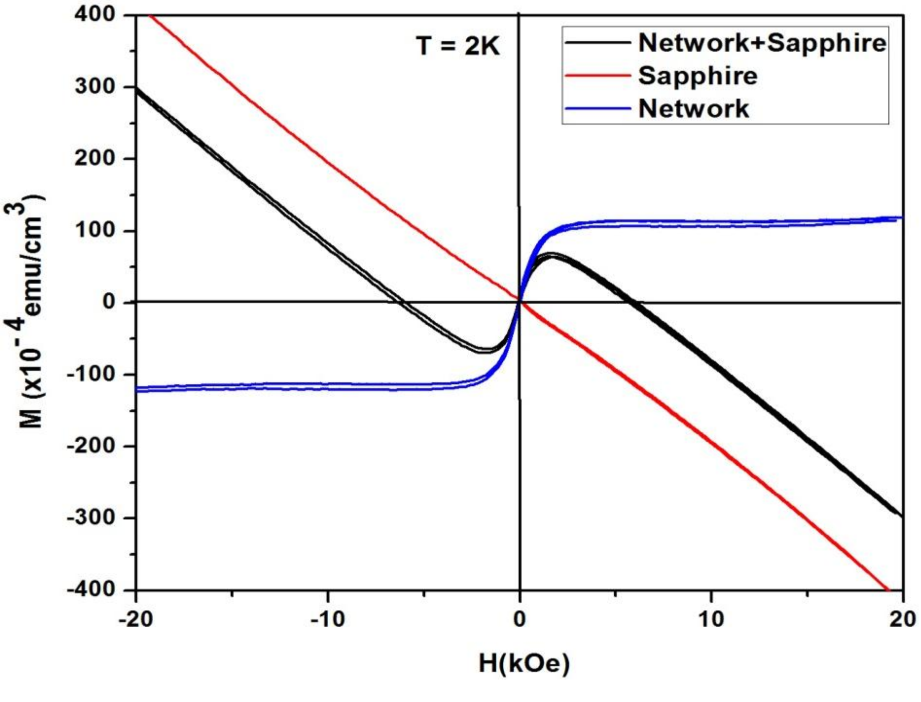

Fig3.18: M-H curve for the GaN nanowall network at T = 2 K, before and after the strong diamagnetic correction for sapphire substrate was employed.

The M-H curves for pure GaN nanowall network at various temperatures are shown in fig.3.19. Saturation in magnetization was not observed for M-H curves at temperatures other than 2 K. This could be due to contribution from paramagnetic centres present in the sample.

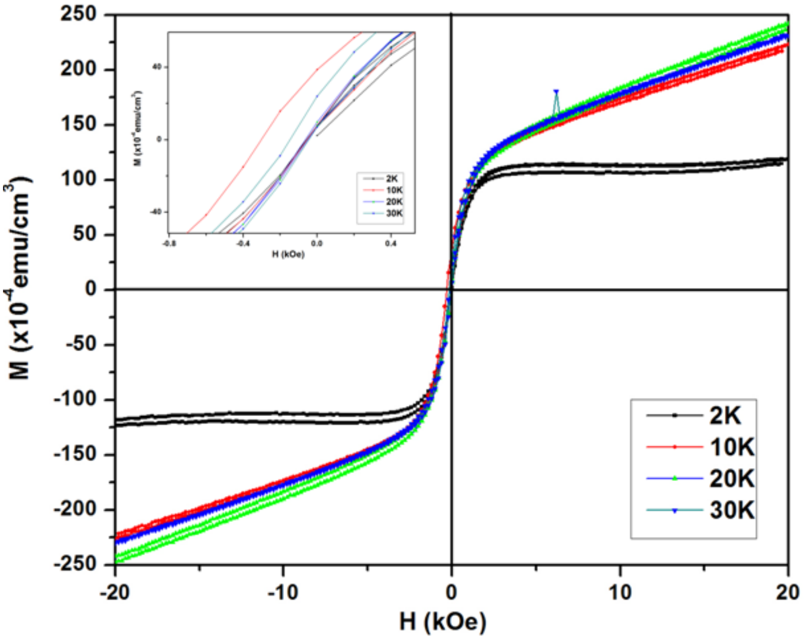

Fig.3.19: M-H curve for the GaN nanowall network at various temperatures

Motivated by this we performed MFM measurements on the film to identify regions contributing to the magnetic moment. Magnetic Force Microscopy (MFM) measurements performed on both network and epilayer showed extremely significant differences (Fig. 3.20). While for GaN epilayer no magnetic region could be seen in the MFM imaging, for nanowall network an excellent magnetic contrast was observed and the apex of nanowalls could be mapped clearly, suggesting that this region of quantum confinement at the nanowall apex is giving rise to ferromagnetism. Fig 3.20 shows the MFM images for the case of epilayer and GaN nanowall network. The width of the nanowall apex was found to be ≈ 30 nm, which agrees well with the results obtained using FESEM and AFM measurements.

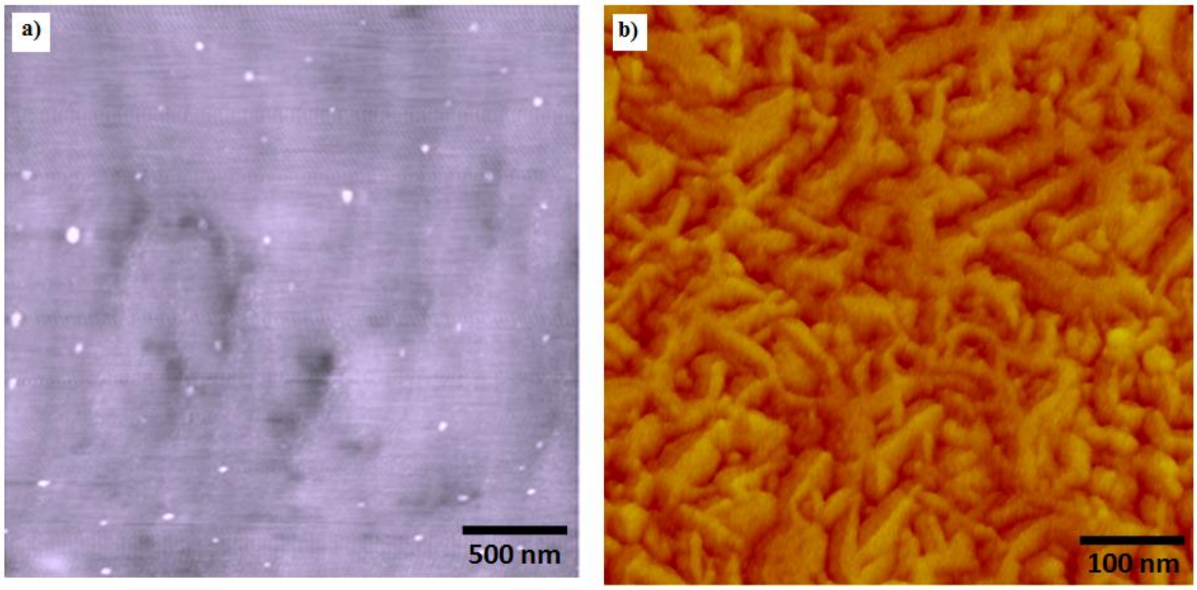

Fig.3.20: MFM contrast as seen for a) GaN Epilayer b) GaN nanowall network

Both Ga and N vacancies are suggested to be present in the as-grown GaN depending on the growth conditions. Calculations of the energies of formation of Ga and N vacancies in bulk GaN have been reported in the literature. Although the formation of nitrogen vacancy has lower energy, electronic structure calculations have shown that this type of vacancy causes a paramagnetic state [38-39, 61]. On the other hand, Ga vacancies introduce magnetic moments which lie on the neighbouring N atoms that are spin polarized due to the Hund's rule. This type of magnetism due to defects in bulk GaN has not been observed because of the large formation energy of defects in bulk GaN. However, the defect formation energy at the surface of the nanostructures may be significantly different from that in the bulk due to the size effect which involves structural as well as electronic effects. Thus, the defect formation energies at the surface are lower, resulting in high concentration of defects at the apex of nanowalls, which gives rise to percolative ferromagnetism at the surface of the GaN nano-network.

A Field Cooled (FC) plot of magnetization as a function of temperature for the nanowall network is shown in fig. 3.21. At fields as low as 50 Oesterds the diamagnetic contribution from the 2 μm sapphire substrate was extremely dominant and it suppressed the signal from the film which was only 0.8 μm in thickness. Finally for a very low applied field of 10 Oe, diamagnetic contribution from the substrate is very low and the M-T curve for nanowall network looked like that of a magnetic material but unlike ferromagnetic materials as no saturation was seen at low temperatures.

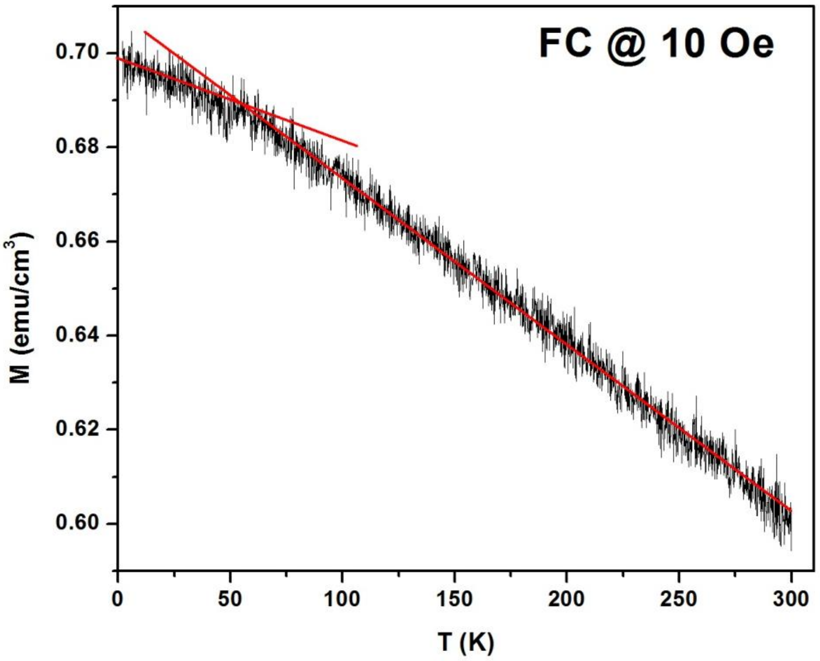

Fig3.21: Field Cooled (FC) M-T curve for the GaN nanowall network at 10 Oe

By carefully inspecting the curve it was seen that a change of slope occurred in the vicinity of T~50 K. The magnetization as a function of temperature indicates many multiple exchange interactions indicating that its decay cannot be easily fit to classical description of ferromagnetism, again in agreement with current theories concerning DMS systems with high carrier concentrations [61, 75, 78]. Similar to the case of (Ga,Mn)N, fitting of this data can be done using mean-field approximation to estimate the curie temperature of GaN in this nanowall network like morphology and further analysis is progressing well in this direction.

Sheet resistivity of the nanowall network was measured as a function of temperature and the film showed very less resistance even at low temperatures ~10K (fig. 3.22). In the absence of an applied magnetic field the GaN nanowall network showed resistivity minimum at 183.19 K and a hump at 380 K. In the light of previously reported results for (Ga,Mn)N this hump at 380 K is suspected to be the Curie temperature for the system, arising probably due to the Extraordinary Hall Effect [74].

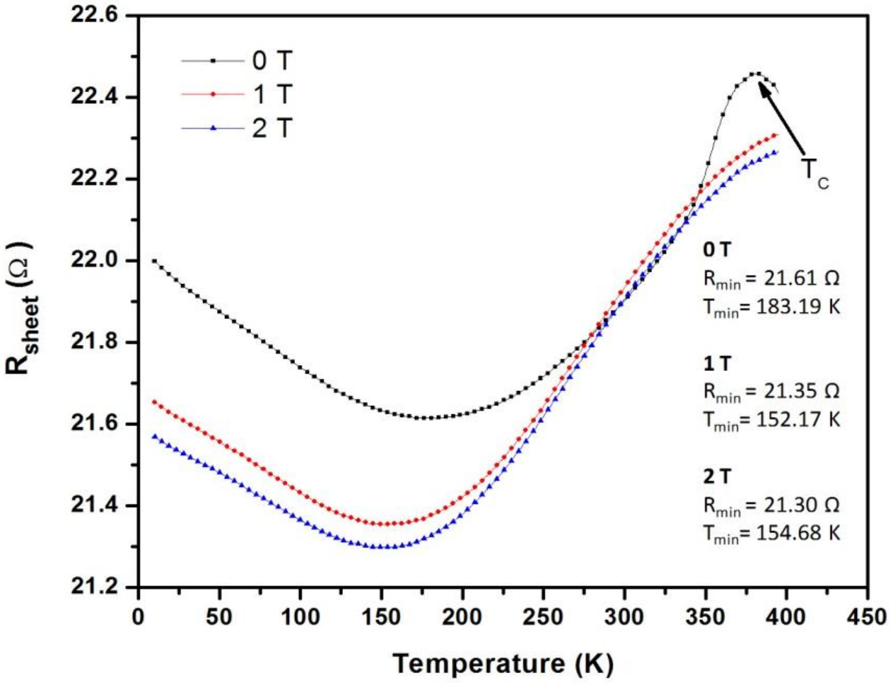

Fig.3.22: Temperature dependence of sheer resistance for the GaN nanowall network at various applied fields

Further, the network was found to posses a negative magneto-resistance ~ -1.5% at temperatures lower than the resistivity minima which diminishes as we approach room temperature. A shift in resistivity minima was also observed with the applied field. The nature of this resistivity minimum is still not clear, as we speculate it could be either of a Kondo like transition (which is a very typical characteristic of DMSs) or a normal metal to semiconductor transition. Further investigations are needed to know the exact underlying mechanism.

For the case of epilayer, sheet resistance was found to be extremely high at low temperatures which decreased greatly as we approached room temperature showing behaviour typical of semiconducting materials (Fig. 2.23). Here also a negative magnetoresistance ~ -5% was observed. Earlier reports have also shown that as grown GaN films by MOCVD and MBE show negative magnetoresiatnce.

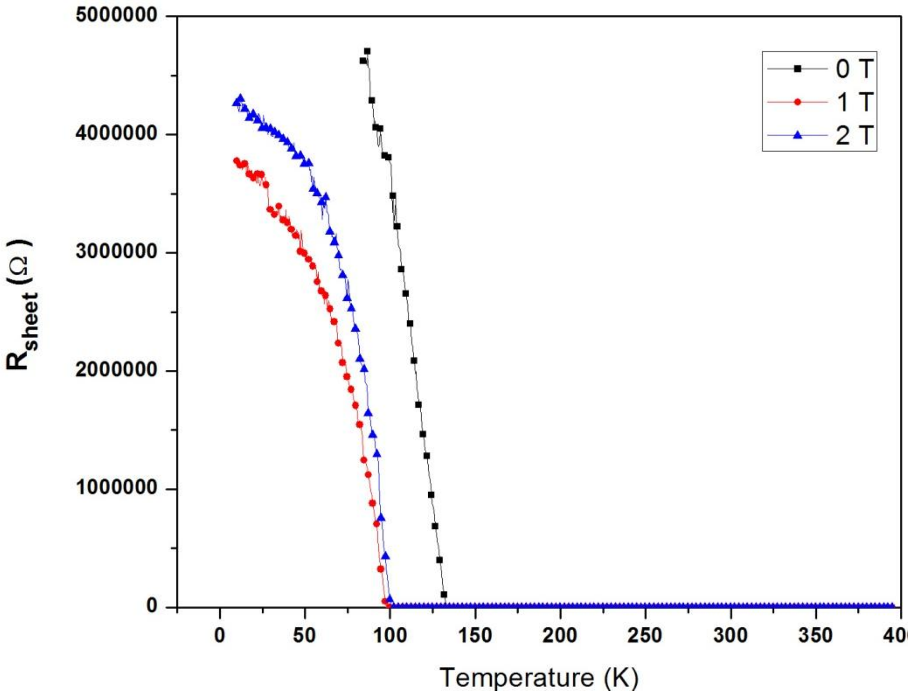

Fig3.23: Temperature dependence of sheer resistance for the GaN epilayer at various applied fields

3.9 Conclusions

GaN nanowall network was found to be ferromagnetic in the low temperature regime and this ferromagnetism saturated at 2 K while at higher temperatures this magnetism did not saturate due to excess paramagnetic centers present in the system. On the other hand GaN epilayer which shows a bulk like behaviour was found to be diamagnetic at all temperatures.

These results could be explained by drawing a parallel from literature, where calculations have shown that the vacancy formation requires a much lower energy on the surface than in the bulk. This is because each atom makes three Ga–N bonds on the surface but four Ga–N bonds in the bulk. Therefore, the native vacancies should be present largely on the surface layer, and the ferromagnetism observed in nonmagnetic nitrides may arise primarily from their surface defects. On the $(10\bar{1}0)$ surface of GaN each Ga(N) atom is bonded to three N(Ga) atoms. Thus, given the ionic description $(Ga3^{+})(N3^{-})$ for GaN, each surface Ga-atom vacancy generates three holes while each surface N-atom vacancy generates three electrons [79]. The three hole states resulting from one Ga-vacancy appear as empty down-spin gap states and each Ga-vacancy leads to a high-spin ground state with magnetic moment of about $3\mu B$.

Since our network has a large open area due to its geometry, larger number of surface defects exist which might contribute to the observed ferromagnetism. However, it is surprising that the magnetism is confined to regions less than 20 nm thick. So it could also be due to electron confinement effects. To probe this further careful and high resolution investigations and theoretical modelling needs to be done, in order to develop a comprehensive understanding of the origin of this morphology dependent magnetism in GaN at nanoscale. This is of importance as it could open up a plethora of applications in the immediate future.

3.10 Thermoelectric Measurements

Thermoelectric (TE) devices convert heat energy directly into electrical energy without any moving parts. The best TE materials for room temperature applications are

Bi_2Te_3-based materials and structures, but their applications are limited because tellurium is scarce, volatile, and toxic [80]. Furthermore, the operational range of these materials is limited to temperatures less than 100°C. Current research in thin-film TE materials without tellurium is concentrating on materials such as Si/Ge, SiGe/Si, and ErAs:InGaAs/ InGaAlAs superlattices, SiGe alloys and trace of nitride alloys [81].

Thin-film TE materials are of great interest because they offer the potential for direct integration of microcoolers/power generators with various photonic and electronic devices. Some of the outstanding features of III–nitrides that are highly attractive for TE applications include the ability for high-power and high-temperature operation, high mechanical strength, stability, and radiation hardness. Recent study shows that high-In-content InGaN alloys could be potentially important TE materials [82].

The quality of a material’s thermoelectric properties are represented by a figure-of-merit (Z), and often expressed as ZT, as this is a temperature dependent characteristic.

$$Z = \frac{\sigma S^2}{\kappa}$$

κ - Total thermal conductivity of the material

σ - Electrical conductivity of the material

α (Seebeck Coefficient μV/K) – Measure of voltage produced by a temperature gradient in the material.

A good thermoelectric material, hence should have a very high value of S and a higher ratio of electrical conductivity to thermal conductivity.

Thermoelectric power generation is explained by a gradient in conduction band energy, across a material. This gradient in conduction band energy is caused by an applied thermal gradient. For homogeneous materials the conduction band energy is directly related to temperature. Electrons on the hot side of a material have greater conduction band energy than those on the cold side producing an EMF. Similar to conduction band energy, valence band energy is also varied across a material with an applied thermal gradient.

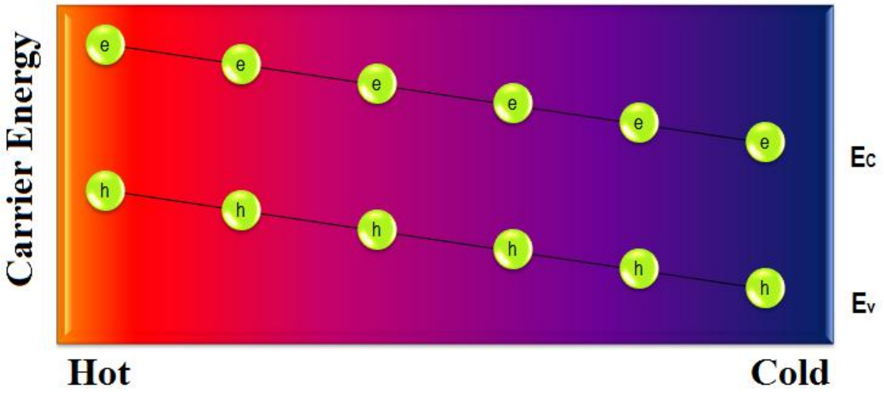

Fig. 3.24: Variation of conduction and valance band energy across a material with thermal gradient

For n-type materials, electrons are the primary charge carriers for which applied thermal gradients produce an EMF in the direction shown below. Redder regions are hotter and Bluish regions are cold regions.

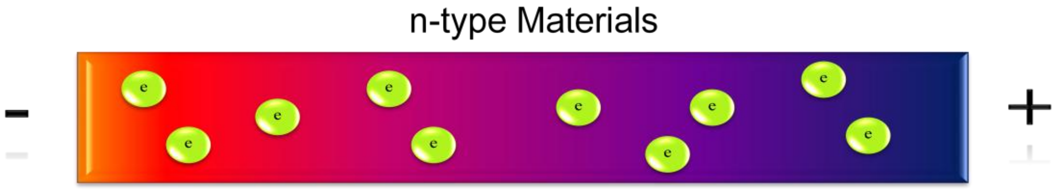

Fig.3.25: flow of charge carrier in a n-type material under thermal gradient

For p-type materials, holes are the primary charge carriers for which applied thermal gradients produce an EMF in the direction shown below.

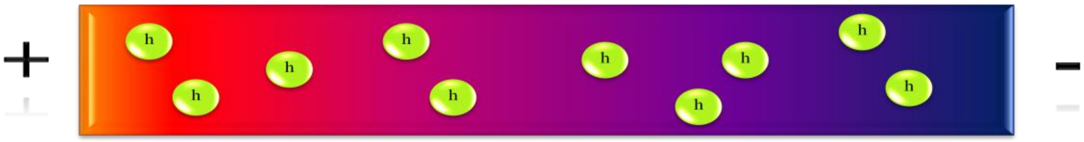

Fig.3.26: flow of charge carrier in a n-type material under thermal gradient

The thermoelectric measurements were done using the homemade handy setup. n-Si and p-Si were used to standardize the setup . And, then measurements were performed on both samples. Here also it was seen that the network as well as epilayer sample showed majority carriers to be electrons, since the applied thermal gradients produced an EMF in the same direction as n-Si. This is clearly evident from the slope of the graphs (fig. 3.27), which gives the Seebeck coefficient for the material.

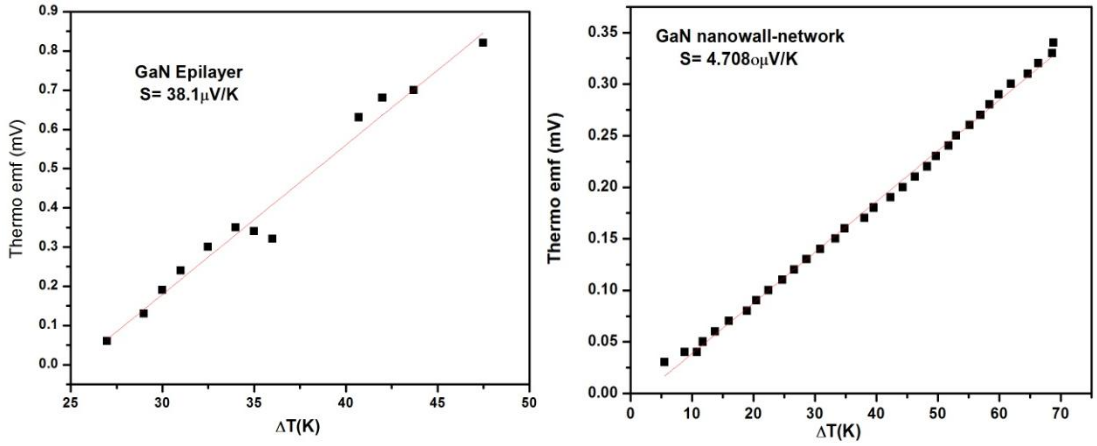

Fig.3.27: Thermo emf as function of temperature difference for a) GaN Epilayer b) GaN nanowall network

Since from Hall measurements, the carrier concentrations for the nanowall network were seen to be very high with a low mobility we expected it to be a good material for thermoelectric applications. But, the Seebeck coefficient for GaN nanowall network was found to be less than that of epilayer.

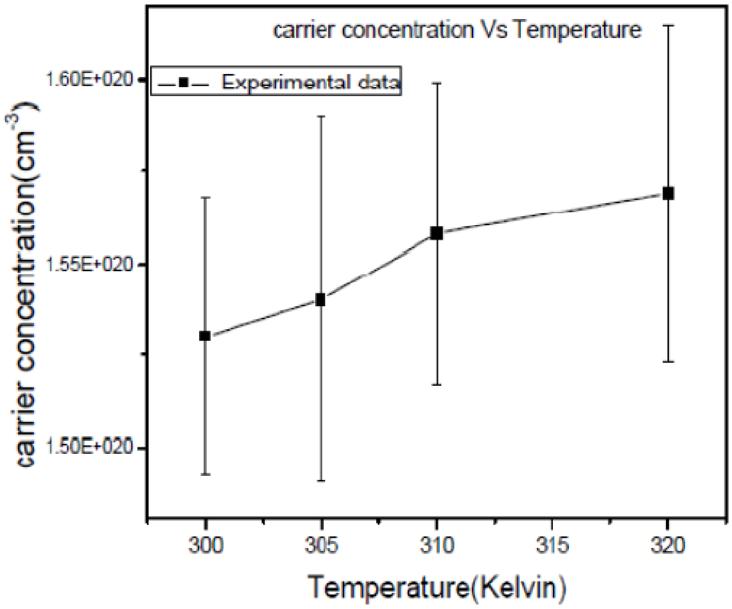

Fig3.28: Temperature variation of carrier concentration for GaN nanowall network

Carrier concentration for nanowall network was found to be almost independent of temperature variations above room temperature indicating that this is a degenerate semiconductor. Carrier concentrations extracted from thermoelectric measurements (Fig. 3.28) compare well with those obtained from Hall measurements. If by some passivation experiments, we can decrease the thermal conductivity of these electrons we can achieve a material with good thermoelectric material for future on chip thermally cooled devices. The morphology of the network shows that by proper engineering we can decrease the thermal conductivity, while having a high carrier concentration, to enhance the Z factor.

Chapter 4

Theoretical Studies

Chapter IV

Theoretical Studies

In this chapter details of various theoretical methods employed to study the GaN/Al_2O_3 interface, the results of simulations done and the future direction of the work is presented.

4.1 Density Functional Theory (DFT)

Density functional theory (DFT) is presently the most successful (and also the most promising) approach to compute the electronic structure of matter. Its applicability ranges from atoms, molecules and solids to nuclei and quantum and classical fluids. In its original formulation, DFT provides the ground state properties of a system, and the electron density plays a key role. Over the years DFT has been used to predict a great variety of material properties like molecular structures, vibrational frequencies, cohesive energies, ionization energies, electric and magnetic properties, reaction paths, etc. With the advancement of computational technologies and physics, the original density functional theory has been successfully generalized to deal with many different situations like spin polarized systems, multi component systems such as nuclei and electron-hole droplets, free energy at finite temperatures, superconductors with electronic pairing mechanisms, relativistic electrons, time-dependent phenomena and excited states, bosons, molecular dynamics, etc [83,84].

From elementary quantum mechanics, we know that the information about a system can be extracted by Schrödinger equation, where ψ captures all material specific properties

$$\hat{H}\,\Psi = E\,\Psi \tag{4.1}$$

Here, E represents the total energy eigenvalue and $\hat{H}$ is the many-body Hamiltonian operator []. This operator can be formulated as

$$\hat{H} = \sum_{i=1}^{N_e} -\frac{\hbar^2}{2m}\nabla_i^2 + \sum_{I=1}^{N_{nuc}} -\frac{\hbar^2}{2M}\nabla_I^2 + \frac{1}{2}\sum_{i\neq j}\frac{e^2}{|r_i - r_j|} - \sum_{i,I}\frac{Z_I e^2}{|r_i - R_I|} + \frac{1}{2}\sum_{i\neq j}\frac{Z_I Z_J e^2}{|R_I - R_J|} \quad (4.2)$$

The first two terms describe the kinetic energy of the electrons and nuclei. The other three terms represent the attractive electrostatic interaction between the nuclei and the electrons and repulsive potential due to the electron-electron and nucleus-nucleus interactions. Here ħ is Planck's constant, Z_I is atomic number of I^{th} atom, r_i and R_I are the position of i^{th} electron and I^{th} nucleus, m and M are the mass of electron and nucleus respectively.

To solve this many-body Schrödinger equation Born-Oppenheimer approximation is employed which states that, since the nuclei are heavier than electrons due to their masses they move much slower than the electrons and hence we can consider the electrons as moving in the field of fixed nuclei. This implies that the nuclear kinetic energy is zero and their potential energy is merely a constant. Hence we can separate the entire wave function into two parts, electronic and ionic part. The Schrödinger equation corresponding to electronic part can be written as

$$H_e\,(r, R)\Psi_e = E_e\,\Psi_e \quad (4.3)$$

The electronic Hamiltonian reduces to

$$\hat{H} = \sum_{i=1}^{N_e} -\frac{\hbar^2}{2m}\Delta_i^2 + \frac{1}{2}\sum_{i\neq j}\frac{e^2}{|r_i - r_j|} + \hat{V}_{ext} \quad (4.4)$$

Here $\tilde{V}_{ext}$ denotes the potential acting on the electrons induced by the nuclei or any externally applied field.

Even after introducing Born-Oppenheimer approximation, it is difficult to solve this equation with available computational resources. Hohenberg-Kohn postulated that this problem can be treated if we use electron density instead of many-body wave function to describe the system of interest. The Hohenberg-Kohn theorems lie in the heart of DFT. As mentioned earlier, the fundamental concept of DFT is to use electron density as an alternative of complicated many-body wave function to handle interacting systems. DFT demands much lesser computational effort and gives a considerably good description of ground state properties of materials [83-85].

The Hohenberg-Kohn theorem states that the ground state electron density ρ_0 minimises the energy functional

$$E[\rho] = \hat{F}[\rho] + \int dr\, V_{ext}(r)\rho(r) \tag{4.5}$$

Where, $\hat{F}$ is a universal functional of ρ and V_{ext} is the potential due to the static ions. Furthermore the minimum value of E is E_0, the ground state electronic energy.

This introduces the concept of electron density as a fundamental variable. If the functional $E[\rho]$ can be minimised with respect to the electron density, it will yield the ground state electronic energy and density of the system. It is important to note that this minimization of the explicit energy functional restricts the calculations based on DFT to the systems in their ground state and the form of the functional $\hat{F}[\rho]$ is not known.

To overcome this Kohn and Sham in 1965, separated the functional F[ρ] into three parts to account for the kinetic energy of a non-interacting electron gas, and the Hartree (Coulomb) and exchange-correlation (XC) effects of the electron-electron interaction. Hence, the total energy functional can be expressed as,

$$E[\rho(r)] = T_s[\rho(r)] + \frac{1}{2}\int \frac{\rho(r)\rho(r')}{|r_i - r'_j|} dr dr' + E_{xc}[\rho(r)] + \int \rho(r)V_{ext}(r)dr \tag{4.6}$$

Where $T_s[\rho(r)]$ is the kinetic energy functional for non-interacting electrons, second term is electrostatic energy, third term is exchange and correlation energy and last is the energy due to external potential caused by nuclei and other externally applied potentials. They showed that the ground state energy could be obtained by solving N one-electron Schrödinger-like equations, self-consistently with the charge density.

$$[\nabla^2 + V_H + V_{xc} + V_{ext}]\Psi_i(r) = \epsilon_i \Psi_i(r) \qquad (4.7)$$

The Hamiltonian of the one-electron equations is of the form of Schrödinger equations but with the potential replaced by an effective KS potential including Hartree and XC parts. Therefore, while the individual solutions do not include inter-particle interactions (one-electron approximation), the KS particles do interact indirectly via the density dependence of the Hartree and XC parts of the potential within a mean-field approximation.

The exchange-correlation potential describes the effects of the Pauli principle and the Coulomb potential beyond a pure electrostatic interaction of the electrons. Possessing the exact exchange-correlation potential means that we solved the many-body problem exactly, which is clearly not feasible in solids. The theory discussed above is exact. However, the functional for XC, given by

$$V_{xc} = \frac{\delta E_{xc}[\rho(r)]}{\delta \rho(r)} \qquad (4.8)$$

is not known for all but a few simple situations (such as a homogeneous free-electron gas).

While DFT in principle gives a good description of ground state properties, practical applications of DFT are based on approximations for the so-called exchange-correlation potential. A common approximation is the so-called local density approximation (LDA) which locally substitutes the exchange-correlation energy density of an inhomogeneous system by that of an electron gas evaluated at the local density [83-

87]. While many ground state properties (lattice constants, bulk moduli, etc.) are well described in the LDA, the dielectric constant is overestimated by 10-40% in LDA compared to experiment. This overestimation stems from the neglect of a polarization-dependent exchange correlation field in LDA compared to DFT. Another approach, the generalized gradient approximation (GGA), also includes the gradient of the density in the calculation.

In the present study, we have used Spanish Initiative for Electronic Simulations with Thousands of Atoms (SIESTA) implementation of DFT, an open source package. Following section gives a brief about SIESTA.

4.2 SIESTA

Siesta (Spanish Initiative for Electronic Simulations with Thousands of Atoms) is both a method and its computer program implementation, to perform electronic structure calculations and *ab-initio* molecular dynamics simulations of molecules and solids. Its main characteristics are [88]:

- It uses the standard Kohn-Sham self-consistent density functional method in the local density (LDA-LSD) or generalized gradient (GGA) approximations.
- It uses norm-conserving pseudopotentials in their fully nonlocal (Kleinman-Bylander) form.
- It uses atomic orbitals as a basis set, allowing unlimited multiple-zeta and angular momenta, polarization and off-site orbitals. The radial shape of every orbital is numerical and any shape can be used and provided by the user, with the only condition that it has to be of finite support, i.e., it has to be strictly zero beyond a user-provided distance from the corresponding nucleus. Finite-support basis sets are the key for calculating the Hamiltonian and overlap matrices in O(N)

operations.

- Projects the electron wavefunctions and density onto a real-space grid in order to calculate the Hartree and exchange-correlation potentials and their matrix elements.
- Besides the standard Rayleigh-Ritz eigenstate method, it allows the use of localized linear combinations of the occupied orbitals (valence-bond or Wannier-like functions), making the computer time and memory scale linearly with the number of atoms. Simulations with several hundred atoms are feasible with modest workstations.
- It is written in FORTRAN 95 and memory is allocated dynamically.
- It may be compiled for serial or parallel execution (under MPI).

4.3 Results

Growth of GaN on sapphire substrates has been extensively studied by experimentalists for decades but a lack of theoretical simulations for the same inspired us to look into the nature of the interface from first-principles perspective. We have performed first-principles total-energy density functional calculations based on the Local Density Approximation (LDA) to study the various geometries of the GaN/Al_2O_3 interface in order to find the most suitable candidate for the interface and hence determine the kinetics for the spontaneous formation of nanostructures . Using repeated free-surface terminated slabs, the relative stability of three different models of the GaN (0001)/Al_2O_3 (0001) interface is examined and the interfacial energy is calculated.

SIESTA implementation of DFT, which uses atomic orbitals as basis set was used to perform all the calculations. We started with the experimentally obtained structures for Al_2O_3 and GaN. Firstly bulk structure optimization calculations were performed for

Al_2O_3 and GaN to test available pseudopotentials and default basis sets. The results were benchmarked with respect to all electron LAPW calculations from literature [1]. While we obtained a very good agreement in the lattice structure for Al_2O_3 with the default basis and available pseudopotentials, the results deviated largely for GaN. We realized that for GaN the default basis cannot be used since 3d electrons in Ga lie close in energy to N-2s electrons. The 3d electrons in Ga hence cannot be treated as core electrons due to the significant role played by their overlap in the bonding [91].

Next, a special basis for GaN was determined by including Ga-3d semicore states. This new basis was constructed using the soft confinement potential proposed by J. Junquera et al [89]. The form of this soft confinement potential is given by

$$V(r) = V_0 \frac{e^{\frac{-(r_c - r_i)}{(r - r_i)}}}{r_c - r} \tag{4.9}$$

Using this new basis set, convergence for GaN was also obtained within the error bar of DFT. Table 4.1 shows the optimized lattice parameters for GaN and Al_2O_3 by our calculations, which are within 2% error with respect to experimental values.

Material	Experimental(Å) [Ref 1-4]			Calculated - LDA (Å)			All electron LAPW (LDA) (Å)		
	a	**c**	**u**	**a**	**c**	**u**	**a**	**c**	**u**
GaN	3.189	5.185	0.377	3.181	5.159	0.374	3.155	5.152	0.377
Al_2O_3	4.785	12.991		4.758	12.931		4.758	12.911	

Table 4.1: Experimental and optimized lattice constants for Bulk GaN and Al_2O_3 [1]

4.3.1 Interface Calculations

Our calculations using density functional theory (DFT) methods based on the Local Density Approximation (LDA) proceed as follows. Firstly, we constructed three GaN/ Al_2O_3 slab geometry configurations, and their interface atomic structures were optimized by full relaxation to zero force positions. Second, we calculate the slab energy difference, E_{slab}, between separated and joined GaN and Al_2O_3 slabs terminated with free surfaces. This was further used to calculate the work of adhesion and the interfacial energy for these configurations.

GaN has a 33% in plane lattice mismatch with c plane of Al_2O_3, which is determined by the following equation: (details given in introduction section of the thesis)

$$\{a_{(GaN)}-a_{(Al2O3)}\}/a_{(Al2O3)} = \sim 33\% \qquad (4.10)$$

It has been observed experimentally that under equilibrium and non equilibrium growths of GaN on Al_2O_3, mostly GaN grows with a 30^o in plane rotation with respect to sapphire [90]. Under certain conditions GaN has been found to grow without the in-plane rotation as well [90]. Hence, to investigate the nature of this interface, three possible configurations of the initial stages of growth were determined.

Configuration 1 consists of straining the GaN overlayer by 33% so as to match the lattice constant of the substrate i.e. Sapphire.

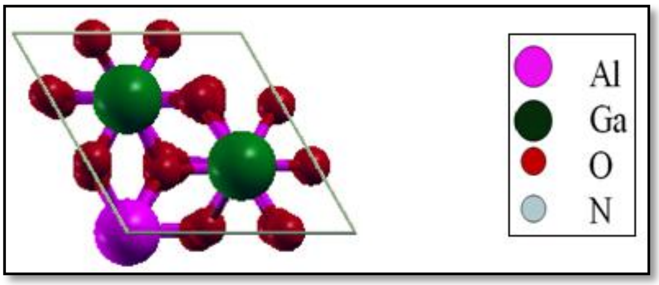

Fig 4.1: Configuration1, depicting the psuedomorpic growth of GaN/Al_2O_3 (1x1 overlap)

Due to large tensile stress in the film, simulations did not relax to a stable structure and we concluded that this is a physically infeasible configuration.

Configuration 2 is defined by putting a 3x3 GaN supercell on 2x2 supercell of Al_2O_3 such that there is a ~0% lattice mismatch at the boundary.

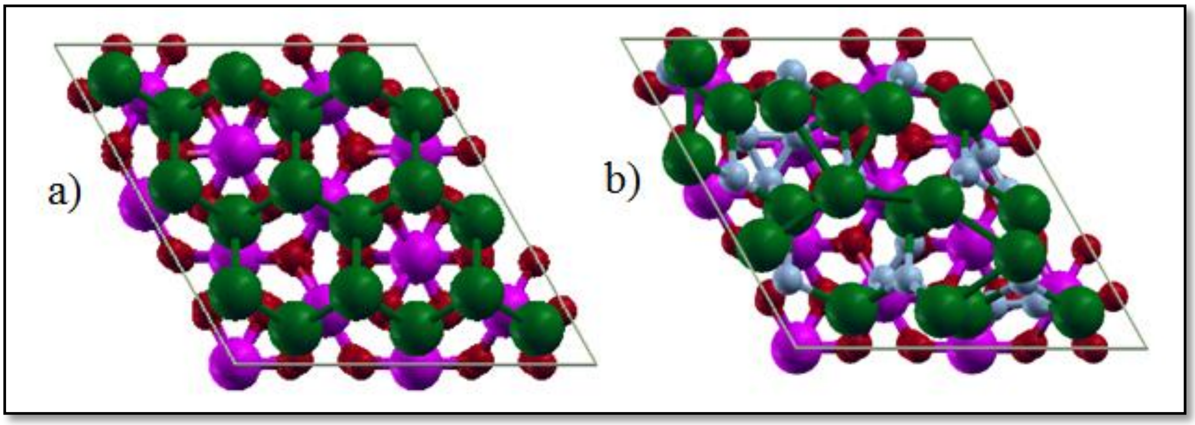

Fig.4.2: Geometry of Configuration 2 (3x3GaN/2x2Al_2O_3) geometry a) before and b) after structural relaxation

This configuration relaxed to an energetically favourable structure and it was seen that the presence of Aluminium in the overlayer causes reconstructions in Nitrogen plane which is evident from fig which shows a side view of the interface.

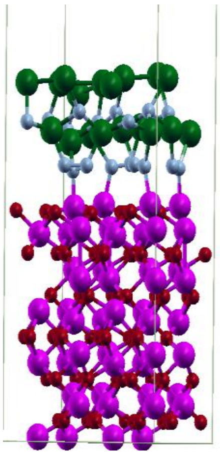

Fig 4.3: Side view of configuration 2 after structural relaxation

Al atoms in the overlayer bind with nitrogen clusters and reconstructions in bond angles and bond lengths span both GaN layers. At the interface Al-N bond length was found to be ~5% smaller than the bulk Al-N bond length. Analysis of bond lengths and bond angles showed that the reconstruction extended in all atomic planes on GaN side of the interface planes and in first three atomic planes for Al_2O_3 side of the interface.

Configuration 3 consists of a GaN unit cell rotated by 30° with respect to the sapphire unit cell, (√3GaN/ Al_2O_3). This geometry results in a reduced lattice mismatch ~16%. Here a 6x6 supercell of GaN on 7x7 supercell of sapphire results in a ~ 0% mismatch at the boundary.

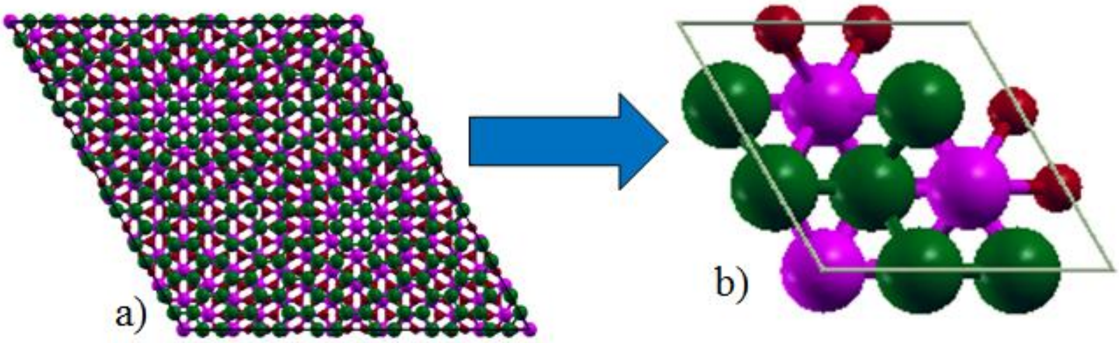

Fig 4.4: Configuration 3 a) showing √3GaN/ Al2O3 geometry and b) the new configuration 3 for computational ease

This particular configuration resulted in an extremely large unit cell containing 1902 atoms. Since such a large supercell was computationally extremely expensive, we decided to incorporate a compression of 16% in the GaN film and leaving the substrate fixed, so as have 1x1 matching at the interface. This is the new configuration 3, wherein √3GaN grows pseudomorphically on Al_2O_3 substrate.

Structural relaxations were done for this configuration with GaN monolayer, bilayer and four layers respectively. For the case of GaN (monolayer) / Al_2O_3, reconstructions in nitrogen layer similar to Configuration 2 are observed. It was seen that three nitrogen atoms cluster on top of overlying Al atom and this charge cloud formed by N atoms bonds with the Al atom, rather than one-to-one bonding.

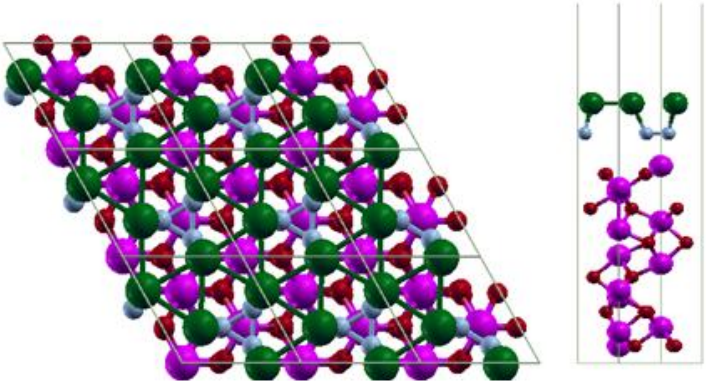

Fig 4.5: Reconstructions as seen in the case of GaN (monolayer)/Al2O3 for Configuration 3

For the case of GaN (bilayer)/Al_2O_3 similar reconstruction was encountered, but the strain relaxation was limited to first two atomic layers only. The second GaN layer was much bulk like with bond lengths and bond angles lying within ~ 10% of the bulk GaN. It was concluded that the reconstruction in N plane helps restrict the reconstruction to first two planes.

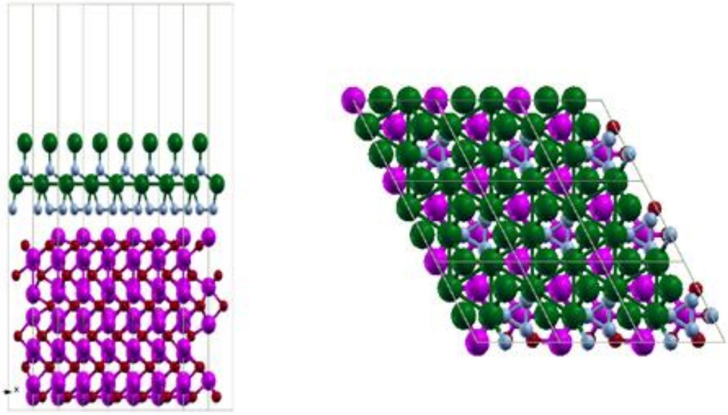

Fig4.6: Reconstructions as seen in the case of GaN (bilayer)/Al2O3 for configuration 3

A comparison of this bilayer Configuration 3 with Configuration 2 shows that this is energetically more favourable. This compares well with the previously reported experimental results that state that the GaN films grow on sapphire substrates with an in plane rotation of 30°.

The interface energy is calculated by consideration of two joined GaN and Al_2O_3 slabs as shown in Fig.4.7. Slab calculations were performed for both GaN and Al_2O_3 and slab energies were calculated as follows.

$$2\ E_{Surf}^{GaN} = E_{slab}^{GaN} - E_{Bulk}^{GaN}$$

$$2\ A\sigma^{GaN} = E_{slab}^{GaN} - E_{Bulk}^{GaN}$$

Where,

σ^{GaN} is surface free energy of GaN

E_{slab}^{GaN} is total free energy for GaN in slab calculations

E_{Bulk}^{GaN} is total free energy for GaN in bulk

A is area of the slabs

Surface energies for Al_2O_3 can also be calculated with similar equations. For a given configuration, work of adhesion of isolated GaN and Al_2O_3 slabs (with free surfaces) is given by

$$\varDelta E_{slab}^{Config} = E_{Tot}^{Config} - (\ E_{Slab}^{GaN} + E_{Slab}^{Al_2O_3}\ )$$

where, E_{Tot}^{Config} is the total free energy for a given configuration.

Interfacial energy is related to this work of adhesion as

$$\varGamma = \frac{\varDelta E_{slab}^{Config}}{A_{slab}}$$

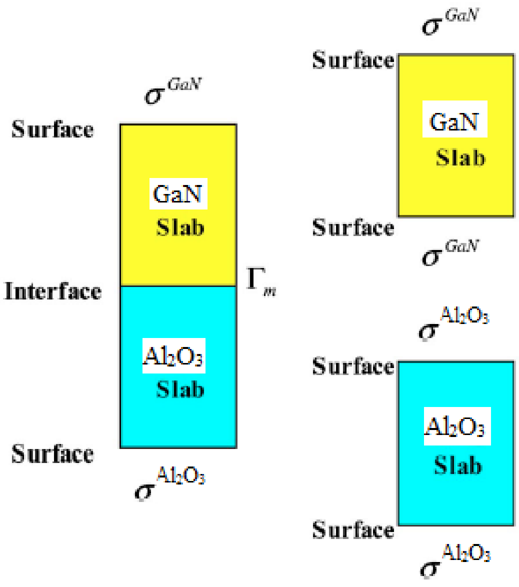
σ^{GaN}
Surface
GaN
Slab
Interface
Γ_m
Al_2O_3
Slab
Surface
$\sigma^{Al_2O_3}$
σ^{GaN}
Surface
GaN
Slab
Surface
σ^{GaN}
$\sigma^{Al_2O_3}$
Surface
Al_2O_3
Slab
Surface
$\sigma^{Al_2O_3}$

Fig 4.7: Slab calculations for the GaN/Al_2O_3 interface

Hence, for Configuration 2 and 3 we have

	Work of Adhesion [ΔE_{slab}^{Config}]	Interfacial energy [Γ]
Config. 2	- 5.52 eV	- 0.061 ev/Å^2
Config. 3	- 9.11 eV	- 0.403 ev/Å^2

Hence we see that the interfacial energy is lower for Configuration 3 than Configuration 2 by ~ 0.34eV/Å^2, implying that configuration 3 is more stable as compared to configuration 2.

4.4. Conclusions

The most favourable interface consists of GaN film having 30° in plane rotation about [0001] with respect to the substrate, which leads to ~14.6 % mismatch for basal plane growth and epitaxial orientation of , (0001)GaN//(0001)Al_2O_3, [11-20]GaN//[10-10]Al_2O_3. This results in reduced lattice mismatch and thus the in-plane strain. Moreover, for this case (configuration 3), work of adhesion is more negative implying that this interface is energetically more stabilized. These findings agree with previously reported experimental results. Plot of charge densities (not shown here) show that covalent bonding between the N-plane and Al- plane exists at the interface.

4.5. Future studies

We aim to perform classical simulations for original Configuration 3 (without compression) to model the evolution of threading dislocations with film thickness and identify the super-structure symmetry of interface dislocations, such that they can be used as nucleation sites for self assembled nanostructure formation. Further we plan to study the evolution of these dislocations with film thickness.

Chapter 5

Conclusions and future directions

Chapter - V

Conclusions and future directions

The GaN thin film with nanowall-network morphology studied in this thesis was grown in plasma assisted molecular beam epitaxy (PA-MBE) system (SVTA, USA) with a base pressure of 2 x 10^{-10} Torr.

Post growth conventional *ex-situ* material characterization by FESEM, XRD and PL were performed to examine the purity of material. The photoluminescence spectra showed a high intensity band edge emission at ≈3.5eV, with a negligible defect band in the proximity of ≈ 2.2eV, comparing well with the literature values for GaN films. XRD pattern of the film confirms the fact that the gallium nitride film was single crystalline and wurtzite in nature and oriented along c-axis. FESEM images showed a hexagonal tri-branched network like morphology.

A second look at these conventional characterizations showed that though the films were pure and highly crystalline, the FWHM of PL band edge and XRD peaks were broad. It was seen that the walls were about 150 nm at the bottom, which tapered down to 10 nm at their apex. This further motivated us to do an in-depth study of the properties of this nanowall network and probe their dependence on this morphology, which lead to further characterizations of electronic structure, electrical, magnetic and thermal transport properties using AFM, MFM, SQUID, I V-Hall measurements etc. The GaN nanowall network showed some interesting properties, which could be credited to its morphology and tapping these properties into practical applications could make it a material of the future.

Through Hall-IV and thermoelectric measurements it was seen that the network shows n-type conductivity with a very high carrier concentration ~ $10^{20}/cm^3$ and a metallic behaviour above 150K. Hence it is a degenerate semiconductor for all temperatures above 150 K at which the system goes through a resistivity minima. The nature of this minima is not yet clear, as it could either be a standard metal-semiconductor type transition or a Kondo like transition due to the magnetic centres present in the film. Even at low temperatures its resistance is ~ a few ohms.

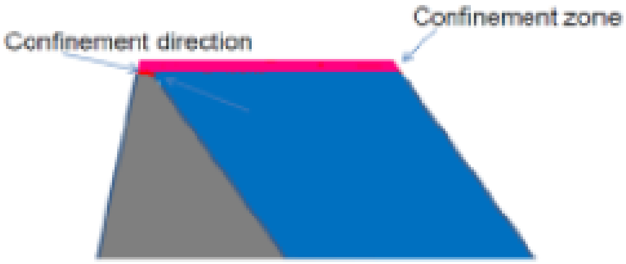

Fig 5.1: Confinement direction in the nanowalls

The apex of the nanowall network is ~ 10-30 nm, which could be a region of strong confinement. Confinement effects were well evident from PL and magnetic measurements. As depicted in the fig.5.1, along the tapered apex of these nanowalls lays the confinement zone in one dimension. This quantum confinement is responsible for some of extremely interesting properties shown by GaN in this particular morphology. For example the surface ferromagnetism which is observed in case of only nanowalls and not the bulk epilayer as shown by MFM images is seen to be lying on these confinement zones. Since, in one dimensional nanostructures, the special topology of the surface and the confinement of electrons in the radial direction drive the coupling to be ferromagnetic

[], during MFM imaging we could map the network very well due to magnetic contributions arising from the apex of these walls which are approximately one dimensional.

The Curie temperature was found to be 380 K, by measuring the temperature dependence of the sheet resistance at zero applied fields, which is seen as a consequence of extraordinary Hall Effect, yet another property that could be attributed to these confinement zones on the nanowall matrix.

This particular nanowall system has been proposed to be a strain relaxed pattern due to its large surface area. This has in turn shown fingerprints in broad luminescence and surface ferromagnetism. Ferromagnetism shown by this nanowall network could be a possible answer to the long standing controversies surrounding the origin of magnetism at nanoscales in otherwise non-magnetic materials. Since these nanostructures are grown under Ultra High Vacuum (UHV) environment, contamination as a possible cause of magnetism can be ruled out and we could say that it is clearly a surface or nano-size related phenomenon. In addition, the magnitude of the magnetic moments can be tuned by changing the size of the nanostructures. The flexibility of both controlling the magnetic coupling and magnetic moment by choosing the dimensionality and the size of the nanostructures will be useful in many practical applications. Further careful and high resolution investigations along with theoretical modelling needs to be done in order to develop a comprehensive understanding of the origin of the present morphology dependent magnetism in GaN at nanoscale. This could open up plethora of applications in near future.

Another powerful application from these nanowall morphologies could be highly coherent and directional emission, which was seen in CL mapping. It was seen that though there is a large distribution in the dimensions of cavity sizes (FWHM of Gaussian fit ~ 120 nm), they emit with approximately the same emission spot size (FWHM of Gaussian fit ~ 36 nm), like a coherent emission. To understand these curious results, we explored the possibility of whispering gallery or Fabry-Perot cavity modes being present in our system, previously shown in similar ZnO nanowall systems . Since, the maxima of the emission lies at the center of the cavities, they do not appear to behave like Whispering gallery micro resonators. Drawing parallel from the Fabry-Perot style resonators that consist of two highly reflecting mirrors with a feedback mechanism; we proposed that the GaN nanowalls with band edge emission also act as highly reflecting mirrors. The narrowness of the top of the walls further aids in focusing the emission and the resultant spot size that is seen is as spherical and extremely intense. This appears to lead towards random lasing without the need of a gain medium in GaN based optoelectronic devices.

In addition to these magnetic and optical properties, GaN based nanostructures posses some outstanding features such as the ability for high-power and high-temperature operation, high mechanical strength, stability, and radiation hardness that make them highly attractive for thermoelectric applications. Since we are proposing our nanowall network as a potential candidate for future spintronics applications, we believe that by passivation or doping if we could decrease the thermal conductivity while maintaining a high electron concentration, we could offer a potential candidate for direct integration of microcoolers/power generators with various photonic and electronic devices. Attempts in this direction are under progress.

Theoretical attempts to understand the origin of these nanostructures showed that the energetically most favourable interface consists of GaN film having 30° in plane rotation about [0001] axis with respect to the substrate, which leads to ~14.6 % mismatch for basal plane growth and epitaxial orientation of - (0001)GaN//(0001)Al_2O_3, [11-

20]GaN//[10-10]Al_2O_3. This results in reduced lattice mismatch and thus the in-plane strain. Moreover, for this case (configuration 3), work of adhesion is more negative implying that this interface is energetically more stabilized. These findings agree with previously reported experimental results. Further it was observed that a reconstruction existed in the N- plane, wherein three N atoms cluster together on the overlying Al atom and bonding at the interface exists between this N cluster and the Al atom. Plot of charge densities show that covalent bonding between the N-plane and Al- plane existing at the interface, results in Al-N interfacial bonds being 10% shorter than the bulk Al-N bonds.

In future we aim to perform classical simulations for $\sqrt{3}$GaN/ Al_2O_3 lattice matched interface (without compression) to model the evolution of threading dislocations with film thickness and identify the super-structure symmetry of interface dislocations; such that they can be used as nucleation sites for self assembled nanostructure formation.

Conclusions and future directions

References

1. Handbook of Nitride Semiconductors and Devices, Hadis Morkoç Volume 1-4, ISBN: 978-3-527-40838-2
2. S. C. Jain1, M. Willander2, J. Narayan3, and R. Van Overstraeten, J. Appl. Phys. **87**, 965 (2000)
3. S. Nakamura and G. Fasol. The Blue Laser Diode. Springer-Verlag, Berlin, 1997.
4. I. Akasaki and H. Amano. Japanese Journal of Applied Physics, 36:5393, 1997.
5. T. Mikai, M. Yamada and S. Nakamura. Japanese Journal of Applied Physics, 38:3976, 1999.
6. S.T. Strite and H. Morkoç, J. Vacuum Science and Technology B10 (1992) 1237
7. B. K. Ridley, J. Appl. Phys. 84(1998) 4020
8. U.V.Bhapkar and M. S. Shur, ibid. 82 (1997) 1649
9. Ambacher, O., Majewski, J., Miskys, C., Link, A., Hermann, M., Eickhoff, M., Stutzmann, M., Bernardini, F., Fiorentini, V., Tilak, V., Schaff, B. And Eastman, L.F. (2002) Pyroelectric properties of Al(In)GaN/GaN heteroand quantum well structures. Journal of Physics: Condensed Matter, 14, 3399–3434.
10. Patrick Rinke, M. Winkelnkemper, A. Qteish, D. Bimberg, J. Neugebauer, and M. Scheffler Physical review B 77, 075202 (2008)
11. Lei, T., Fanciulli, M., Molnar, R.J., Moustakas, T.D., Graham, R.J. and Scanlon, J. (1991) Applied Physics Letters, 59, 944.
12. Paisley, M.J., Sitar, Z., Posthill, J.B. and Davis, R.F. (1989) Journal of Vacuum Science & Technology, 7, 701.
13. Powell, R.C., Lee, N.E., Kim, Y.W. and Greene, J.E. (1993) Journal of Applied Physics, 73, 189.

14. Mizita, M., Fujieda, S.,Matsumoto, Y. And Kawamura, T. (1986) Japanese Journal of Applied Physics, 25, L945.
15. Leszczynski, M. (1999) Common crystal structure of the group III-nitrides, in Properties, Processing and Applications of Gallium Nitride and Related Semiconductors (eds J.H. Edgar, S. Strite, I. Akasaki, H. Amano and C.Wetzel), EMIS Data Review Series, No. 23, INSPEC, The Institution of Electrical Engineers, Stevenage, UK, pp. 3–5.
16. Ambacher, O., Majewski, J., Miskys, C., Link, A., Hermann, M., Eickhoff, M., Stutzmann, M., Bernardini, F., Fiorentini, V., Tilak, V., Schaff, B. And Eastman, L.F. (2002) Pyroelectric properties of Al(In)GaN/GaN heteroand quantum well structures. Journal of Physics: Condensed Matter, 14, 3399–3434.
17. Leszczynski, M., Suski, T., Perlin, P., Teisseyre, H., Grzegory, I., Bockowski, M., Jun, J., Porowski, S., Pakula, K., Baranowski, J.M., Foxon, C.T. and Cheng, T.S. (1996) Applied Physics Letters, 69, 73.
18. Jeffery, G.A., Parry, G.S. and Mozzi, R.L. (1956) Journal of Chemical Physics, 25, 1024.
19. L. Liu, J.H. Edgar , Volume 37, Issue 3, 30 April 2002, Pages 61–127, Materials Science and Engineering: R: Reports
20. B. Monemar, Phys. Rev. B 10, 676–681 (1974)
21. Wu, J., Walukiewicz, W., Yu, K.M., Ager, J.W., III, Haller, E.E., Lu, H., chaff,W.J., Saito, Y. and Nanishi, Y. (2003) Applied Physics Letters, 80, 3967.
22. Jithesh Kuyyalil, Malleswararao Tangi, and S. M. Shivaprasad, J. Appl. Phys. 109, 093513 (2011)
23. P. Vennegues, B. Beaumont, and P. Gibart, Phys. Status Solidi 227, 1 (2001).

24. P. Kumar, J. Kuyyalil, and S. M. Shivaprasad, Appl. Phys. Lett. 97,221913 (2010).
25. R. Colby, Z. Liang, I. H. Wildeson, D. A. Ewoldt, T. D. Sands, R. E. Garcı`a, and E. A. Stach, Nano Lett. 10(5), 1568 (2010).
26. M. Elison and W. Claude, J. Phys. D: Appl. Phys. 43, 354005 (2010).
27. F. Qian, S. Gradecak, Y. Li, C. Y. Wen, and C. M. Lieber, Nano Lett. 5, 2287 (2005).
28. L. Geelhaar, C. Cheze, W. M. Weber, R. Averbeck, H. Riechert, T. Kehagias, P. Komninou, G. P. Dimitrakopulos, and T. Karakostas, Appl. Phys. Lett. 91, 093113 (2007).
29. R. Songmuang, O. Landre, and B. Daudin, Appl. Phys. Lett. 91, 251902 (2007).
30. E. Calleja, J. Ristic, S. Fernandez-Garrido, L. Cerutti, M. A. Sanchez- Garcia, J. Grandal, A. Trampert, U. Jahn, G. Sanchez, A. Griol, and B. Sanchez, Phys. Status Solidi B 244, 2816 (2007).
31. Manoj Kesaria and S. M. Shivaprasad , Appl. Phys. Lett 99, 143105 (2011).
32. Manoj Kesaria, Satish Shetty, and S. M. Shivaprasad, Cryst. Growth Des. 2011, 11, 4900–4903.
33. http://serc.carleton.edu/research_education/geochemsheets/techniques/SEM.html
34. http://www.purdue.edu/rem/rs/sem.htm
35. http://en.wikipedia.org
36. http://micron.ucr.edu/public/manuals/EDS-intro.pdf
37. http://ned.ipac.caltech.edu/level5/Sept03/Li/Li4.html
38. J. Neugebauer and Chris G. Van de Walle, Phys. Rev. B 50, 8067 (1994)
39. Chris G. Van de Walle, J. Neugebauer J. Appl. Phys. 95, 3851 (2004)

40. Semiconductors And Semimetals, Gallium Nitride (GaN) , Jacques I. Pankove, Theodore D. Moustakas, 0-12-752166-6, 1999 By Academic Press
41. N.J. Suthan Kissinger, M. Jayachandran, K. Permual, C. Sanjeevi Raja Bull. Mater. Sci., 30 (2007), p. 547
42. III-V Nitride Semiconductors: Defects and Structural Properties M.O. Manasreh (Ed.) , 2000 Elsevier Science
43. M. Leroux, B. Gil, In: J.H. Edgar, S. Strite, I. Akasaki, H. Amano, C Wetzel (Eds.), GaN and Related Semiconductors, EMIS Datareviews Series No. 23, INSPEC, London, 1999, p. 62.
44. B. Gil, M. Leroux, In: J.H. Edgar, S. Strite, I. Akasaki, H. Amano, C Wetzel (Eds.), GaN and Related Semiconductors, EMIS Datareviews Series No. 23, INSPEC, London, 1999, p. 68.
45. B. Monemar, In: S.J. Pearton (Ed.), Optoelectronic Properties of Semiconductors and Superlattices, Vol. 2, Gordon and Breach, Amsterdam, 1997, pp. 95.
46. N. Grandjean, J. Massies, M. Leroux and P. Lorenzini, Appl. Phys. Lett. 72, 82 (1998).
47. R. Dingle and M. Ilegems, Solid State Commun. 9, 175 (1971).
48. S. Ficher, C Wetzel, E.E. Haller and B.K. Meyer, Appl. Phys. Lett. 67, 1298 (1995).
49. O. Lagerstedt and B. Monemar, J. Appl. Phys. 45, 2266 (1974).
50. M. Leroux, B. Beaumont, N. Grandjean, P. Gibart, J. Massies and J.P. Faurie, MRS Internet J. Nitride Semicond Res. 1, 25 (1996).
51. T. Ogino and M. Aoki, Jpn. J. Appl. Phys. 19, 2395 (1980).
52. T, Suski, P. Perlin, H. Teisseyre, M. Leszczynski, L Grzegory, J. Jun, M. Bockowski, S. Porowski and T.D. Moustakas, Appl. Phys. Lett. 67, 2188 (1995).

53. C.G. Van der Walle and J. Neugebauer, Mat. Res. Soc. Symp. Proc. 449, 861 (1997).
54. Chen, H.M., Chen, Y.F., Lee, M.C. and Feng, M.S. (1997) Physical Review B: Condensed Matter, 56, 6942.
55. Reshchikov, M.A. and Korotkov, R.Y. (2001) Physical Review B: Condensed Matter, 64, 115205.
56. V. Loo, L. Lanco, O. Krebs, P. Senellart, P. Voisin Phys. Rev. B 83, 033301 (2011).
57. V. Loo, L. Lanco, A. Lemaître, I. Sagnes, O. Krebs, P. Voisin, P. Senellart, Appl. Phys. Lett. 97, 241110 (2010)
58. Z. Mi, S. Vicknesh, F. Li, and P. Bhattacharya , Proceedings of SPIE 7220, 72200S (2009)
59. Yang Zhang, Weifeng Zhang and C. Peng, Vol 16, No 14, Optics Express 10696, (2008)
60. Daniel J. Gargas, Michael C. Moore, Adrian Ni, Shu-Wei Chang, Zhaoyu Zhang, Shun-Lien Chuang and Peidong Yang, ACS Nano, 2010, 4 (6), pp 3270–3276
61. Zhihua Xiong, Lan Luo,, Jianfei Peng , Guodong Liu, Journal of Physics and Chemistry of Solids Volume 70, Issue 8, August 2009, Pages 1223‐1225
62. Basanta Roul, Mohana K. Rajpalke, Thirumaleshwara N. Bhat, Mahesh Kumar, A. T. Kalghatgi, S. B. Krupanidhi, Nitesh Kumar and A. Sundaresan, Appl. Phys. Lett., 99, 162512 - 162514 (2011)
63. A. Sundaresan, R. Bhargavi, N. Rangarajan, U. Siddesh, and C. N. R. Rao, Physical Review B 74, 161306(R) (2006)
64. A. Sundaresan, C.N.R. Rao, Nano Today (2009) 4, 96 - 106

65. C. Madhu, A. Sundaresan, and C. N. R. Rao, Physical Review B 77, 201306 (R) (2008)
66. J. M. D. Coey, M. Venkatesan & C. B. Fitzgerald, Nature Materials 4, 173 - 179 (2005)
67. J.M.D. Coey and S.A. Chambers, MRS Bulletin November 2008 33 : pp 1053-1058
68. M. Venkatesan, C. B. Fitzgerald & J. M. D. Coey, Nature 430, 630 (5 August 2004)
69. J M D Coey, P Stamenov, R D Gunning, M Venkatesan and K Paul, New Journal of Physics 12 (2010) 053025
70. Tatiana Makarova, "Nanomagnetism in Otherwise Nonmagnetic Materials" Handbook of Nanophysics (HNP), Klaus D. Sattler (Editor), published by Taylor & Francis (CRC Press)
71. I. T. Ferguson, phys. stat. sol. (c) 4, No. 2, 389– 396 (2007)
72. K Laaksonen, M G Ganchenkova and R M Nieminen, J. Phys.: Condens. Matter 21 (2009) 015803.
73. S.J. Pearton, C.R. Abernathy, D.P. Norton, A.F. Hebard, Y.D. Park, L.A. Boatner, J.D. Budai Materials Science and Engineering R 40 (2003) 137–168.
74. M. L. Reed, N. A. El-Masry,a) H. H. Stadelmaier, M. K. Ritums, and M. J. Reed, C. A. Parker, J. C. Roberts, and S. M. Bedair, Appl. Phys. Lett.Vol. 79, No. 21 (2001)
75. J.M.D. Coey, Solid State Sciences Volume 7, Issue 6, June 2005, Pages 660‑667
76. P. Xiong, G. Xiao, J.Q. Wang, J.Q. Xiao, J.S. Jiang, and C.L. Chien, Phys. Rev. Lett. 69, 3220 (1992)

77. M.L. Reed, N.A. El-Masry, H. Stadelmaier, M.E. Ritums, N.J. Reed, C.A. Parker, J.C. Roberts, S.M. Bedair, Appl. Phys. Lett. 79 (2001) 3473.
78. Aron Walsh, Juarez L. F. Da Silva, and Su-Huai Wei , Phys. Rev. Lett. 100, 256401 (2008)
79. Hao Jin, Ying Dai, BaiBiao Huang, and M.-H. Whangbo, Appl. Phys. Lett. **94**, 162505 (2009)
80. Rama Venkatasubramanian, Edward Siivola, Thomas Colpitts & Brooks O'Quinn, Nature 413, 597-602 (11 October 2001)
81. J. M. Zide, D. O. Klenov, S. Stemmer, A. C. Gossard, G. Zeng, J. E. Bowers, D. Vashaee, and A. Shakouri, Appl. Phys. Lett. **87**, 112102 (2005)
82. B. N. Pantha, R. Dahal, J. Li1, J. Y. Lin, H. X. Jiang, and G. Pomrenke, Appl. Phys. Lett. **92**, 042112 (2008)
83. W. Kohn, An essay on condensed matter physics in the twentieth century, Reviews of Modern Physics, Vol. 71, No. 2, pp. S59-S77.
84. R.MR.M. Martin. “Electronic Structure: Basic Theory and Practical Methods”. (Cambridge University Press, Cambridge, 2004)
85. M. C. Payne et al. “Iterative minimization techniques for ab-initio total energy calculations”. Review of Modern Physics 64, 1045 (1992).
86. R. O. Jones & O. Gunnarson. “The density functional formalism, its application and prospects”. Review of Modern Physics 61, 689 (1989).
87. J.P. Perdew & A. Zunger, Phys. Rev. B 23, 5048 (1981)
88. José M Soler et al 2002 J. Phys.: Condens. Matter 14 2745
89. J. Junquera et al , Phys. Rev. B. 64, 235111 (2001)
90. N. Grandjean, J. Massies, P. Vennéguès, M. Laügt, and M. Leroux, Appl. Phys. Lett. **70**, 643 (1997)

References

91. Patrick Rinke *et al* 2005 *New J. Phys.* 7, 126